Meteorol Atmos Phys 85, 235–263 (2004)
DOI 10.1007/s00703-003-0009-z

Meteorology and Atmospheric Physics

Printed in Austria

[1] Cloud Physics Research Division, Meteorological Service of Canada, Toronto, Ontario
[2] National Environmental Satellite, Data, and Information Service, National Oceanic and Atmospheric Administration, Madison, WI
[3] NOAA/Environmental Technology Laboratory, Boulder, CO
[4] NASA Goddard Space Flight Center, Greenbelt, MD
[5] Air Quality Processes Research Division, Meteorological Service of Canada, Egbert, Ontario

Dynamical and microphysical characteristics of Arctic clouds using integrated observations collected over SHEBA during the April 1998 FIRE.ACE flights of the Canadian Convair

I. Gultepe[1], G. A. Isaac[1], J. Key[2], J. Intrieri[3], D. O'C. Starr[4], and **K. B. Strawbridge[5]**

With 12 Figures

Received November 28, 2001; revised February 21, 2002; accepted January 13, 2003
Published online: November 28, 2003

Summary

The purpose of this study is to better understand the dynamical and microphysical processes within Arctic clouds, which occurred in April 1998 over the Surface Heat Budget of the Arctic Ocean (SHEBA) ship during the First ISCCP (International Satellite Cloud Climatology Project) Regional Experiment Arctic Cloud Experiment (FIRE.ACE). The observations from the four cases in the present study were collected by instruments mounted onboard the National Research Council (NRC) Convair, as well as, the National Oceanic and Atmospheric Administration (NOAA) Advanced Very High Resolution Radiometer (AVHRR) satellite, the SHEBA surface based NOAA Doppler radar (35 GHz, Ka-Band), and the NOAA depolarization lidar (0.523 μm) measurements. The aircraft observations were collected at 32 Hz (3-m scale). The Meteorological Services of Canada (MSC) lidar (1.064 μm) was operated onboard the Convair-580. The AVHRR observations, representing a 5-km horizontal resolution, were used to estimate particle size, phase, and optical thickness. Constant altitude flight legs were made at about 100 m over the ocean surface. Vertical air velocity (w), reflectivity and Doppler velocity, and backscatter and depolarization ratio values were used to define the size of the important dynamical structures. Ice crystal number concentration (N_i), ice water content (IWC), droplet number concentration (N_d), liquid water content (LWC) and characteristic particle size and shape were summarized for each case. The effective radius (r_{eff}) values for liquid clouds obtained from in-situ and AVHRR observations were found comparable. The large variability in IWC can be due to undetected ice crystals at small size ranges. Mixed phased conditions in the AVHRR retrievals complicated the comparisons with in-situ data. N_i was found to be directly related to the history of the air-parcel dynamics e.g., w. The variability and differences in the parameters obtained from various platforms can be attributed to their instrumental capabilities, resolution, as well as the cloud development.

1. Introduction

The formation and development of Arctic clouds are related to local and large-scale meteorological conditions. The microphysical and dynamical processes can play an important role in cloud development, and affect the Earth's atmospheric heat and moisture budgets that are an important part of the hydrological cycle. Observations over the Arctic ocean in the past were restricted due to limitations in the airborne instruments and the lack of surface observations (Curry et al, 1996; 2000; Randall et al, 1998). The scientific objectives of FIRE.ACE (First ISCCP (International Satellite Cloud Climatology Project) Regional Experiment. Arctic Cloud Experiment) were to study impacts of Arctic clouds on the radiation and surface conditions, and document cloud parameters, including particle size, concentration, and phase as atmospheric conditions change (Curry et al, 2000).

The formation of continental polar air depends on the physical and thermodynamic characteristics of the Earth's surface in the airmass source region (Curry, 1983). Gultepe and Isaac (2002) stated that the characteristics of Arctic clouds are related to whether their airmasses originated from either the Arctic or Pacific Oceans. Murad and Walter (1996), and Schnell et al (1989), using observations from an Arctic field program, suggested that cold-air breaks from further north during wintertime result in large changes in the microphysical, dynamical, and thermodynamical conditions within the Arctic boundary layer. Curry et al (1996), and Kantha (1995) suggested that northerly cold winds coming over polynyas could result in strong latent heat fluxes (LHF) and sensible heat fluxes (SHF), likely effecting cloud development. On the other hand, winds coming from the south may not be as effective as northerly ones because of smaller temperature differences between the ocean surface and the air above.

The Global Energy and Water Experiment (GEWEX News, 1997) working group indicated that cloud dynamical activity should be studied in detail and related to microphysical and radiation parameters. Arctic clouds in transition seasons can have both water and ice particles. It has been observed in earlier field projects (e.g., Gultepe et al, 2000) that these clouds can have substantial dynamical structures that enhance cloud life-time. Embedded cells within the stratiform clouds were found to be common. Vertical air velocities (w) within clouds related to frontal systems occur between -2 and $2\,\mathrm{m\,s^{-1}}$ but only $\pm 0.2\,\mathrm{m\,s^{-1}}$ in stable conditions (Gultepe et al, 2000). A wavelet analysis of dynamical parameters and reflectance from satellite observations indicated that Arctic clouds can have significant heat/moisture fluxes related to dynamical activity (e.g. vertical air velocity fluctuations, w'). Serreze et al (1992) found that open leads can significantly change the boundary-layer height and cloud microphysical structures within it. Heymsfield (1977) stated that ice crystal microphysical parameters within cirrus, e.g. shape and size, are related to w. Pinto and Curry (1995), using a meso-scale model, stated that interactions between large-scale dynamic and cloud processes are important for Arctic cloud development. McInnes and Curry (1995), using a high resolution 1D model, explained that $w \sim 1\,\mathrm{cm\,s^{-1}}$ can be sufficient to maintain cloud life time. Although these studies indicated that cloud dynamical activity is an important parameter, there were no detailed studies to determine the characteristics of dynamical processes and parameters that can be important in cloud microphysical development.

One of the main objectives of the FIRE.ACE and SHEBA experiments is to produce an integrated dataset that provides in-situ data for testing of satellite and ground-based remote sensing analyses, and supports the analysis and interpretation of physical processes within Arctic clouds (Randall et al, 1998). The main objective of the present work is to compare in-situ observations with those retrieved from the remote sensing platforms. During FIRE.ACE in April 1998, the Canadian Convair-580 could only make 4 flights over the Surface Heat Budget of the Arctic Ocean (SHEBA) ship. Using observations from multiple platforms, the present work summarizes the dynamical and microphysical processes that occurred in the Arctic boundary layer during those flights. The size of cells will be estimated from vertical air velocity fluctuations, and will be supported with other observations from remote sensing platforms. The microphysical parameters will be given over constant altitude flight legs and along spirals just above the ocean surface. In the concluding remarks, interactions of microphysical and dynamical/thermodynamical cloud processes and integrated results will be investigated.

2. Observations

The observations obtained for 16, 17, 21, and 28 April 1998 during the Canadian Convair-580

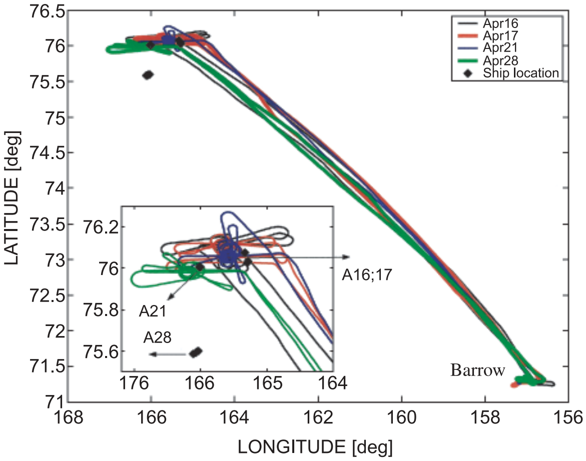

Fig. 1. NRC Convair-580 flight tracks over SHEBA ship for four cases during FIRE.ACE

flights over the SHEBA site are used in the present study. Detailed information on the FIRE.ACE and SHEBA field projects can be found in Gultepe et al (2002), and Curry et al (2000). Figure 1 shows the plan-view of aircraft flight tracks and the locations of the Canadian Coast Guard ice breaker Des Groseilliers (SHEBA ship). The NOAA lidar, and Doppler radar located on the ship were used to obtain measurements related to clouds. NOAA AVHRR observations available for 17, 21, and 28 April were also collected for studying the cloud microphysical and optical parameters.

2.1 Aircraft observations

The Canadian NRC Convair 580 aircraft operated from Inuvik in the Northwest Territories of Canada, and made observations over the Beaufort Sea (~70N:134W), over the SHEBA ship, and along transects across the Beaufort Sea and between Barrow and the SHEBA ship. Table 1 shows the aircraft and remote sensing time periods for data collection. The 32 Hz observations of wind, temperature, and mixing ratio measurements were used in the analysis. The following subsections summarize the aircraft observations.

The droplet number concentration (N_d) and ice crystal number concentration (N_i) were obtained at size ranges of 2–47 and 5–95 μm from two Particle Measuring Systems (PMS) Forward Scattering Spectrometer Probes ($FSSP_{96}$-100 and $FSSP_{124}$-100), and at 25–800 μm from the two-dimensional cloud (2DC) probe measurements, respectively. The subscripts represent two size ranges for FSSP-100. FSSP measurements were corrected for probe dead time and coincidence, and the uncertainty in the sizing and concentration from this probe can be as large as 30% (Baumgardner et al, 1990). Details of the 2D-probe measurements and image-processing techniques can be found in Heymsfield and Parrish (1978). Using measurements from the optical and hot-wire probes, and the Rosemount icing detector (Cober et al, 2000), which responds clearly to liquid phase present within the cloud, discrimination between the ice and water regions within the cloud was accomplished. Note that small N_d with small sized droplets cannot always be detected with this Rosemount icing probe. This uncertainty is not considered here (Strapp et al, 1999; Gultepe et al, 2001a). Temperature (T) was measured by a reverse flow temperature probe with an accuracy of $\pm 0.5\,°C$. The dew point temperature (T_d) was measured by both an EG&G dew-point and a LiCor hygrometer. These measurements were used to calculate the relative humidity with respect to ice (RH_i) (Gultepe et al, 2002). The T_d from the EG&G measurements can be highly unreliable at colder temperatures ($< -20\,°C$). The liquid water content (LWC) was obtained from measurements of the King (Biter et al, 1987), FSSP-100 (Baumgardner et al, 1990), and Nevzorov probes (Korolev et al, 1999). The aerosol number concentrations (N_a) in the range of 0.135

Table 1. Time periods for various platforms used in the analysis. Aircraft and ship locations are given in Fig. 1

Cases	Aircraft [UTC]	MSC lidar [UTC]	WPL radar [UTC]	WPL lidar [UTC]	AVHRR [UTC]
April 16	2025-0058	2212-2218	2200-2400	1808-2340	–
April 17	1827-2300	2012-2018	1400-1600	1400-2300	2400
April 21	2117-0156	2302-2309	2000-2400	2118-0200	2400
April 28	2206-0240	0040-0119	1700-0200	2248-0100	2400

to 3 μm diameter in 15 size bins (Liu et al, 1996) were obtained from Particle Measuring Systems PMS passive cavity aerosol spectrometer probe (PCASP-100x) measurements.

Horizontal and vertical wind components (U_h and w) and horizontal wind direction (D_{uh}) were made using a wing-mounted Rosemount 858 5-hole pressure probe and a Litton LTN-90-100 Inertial Reference System (Williams and Marcotte, 1999). The root-mean square (rms) error for w is estimated at about $0.15\,m\,s^{-1}$. The flight speed for the Convair was approximately $85\,m\,s^{-1}$. Both latitude and longitude were obtained with Marconi and Northstar Global Positioning Systems (rawinsonde) mounted on the Convair. The absolute accuracy of this system is about 10 m. Williams and Marcotte (1999) estimated that, during rapid maneuvers, the uncertainty in w is estimated to be about $0.4\,m\,s^{-1}$.

The LANDSAT simulator developed by Exotech Incorporated, which is used for detecting ocean surface conditions, had four channels (0.46–0.52; 0.52–0.60, 0.63–0.69; 0.76–0.90 μm) similar to the LANDSAT thematic mapper (TM). It has a field of view of 1-degree and an absolute accuracy of about 5%. The channel 1 voltage values from the LANDSAT simulator were used to obtain reflected radiance values (R_{ch1}). LANDSAT simulator measurements are calibrated against the Arizona (AZ) radiometer measurements that were calibrated in a laboratory setting.

2.2 Satellite observations

Estimates of cloud particle phase, optical depth, and particle effective radius for both water and ice phase were obtained from the visible and thermal channels of the Advanced Very High Resolution Radiometer (AVHRR) on board the NOAA-14 polar-orbiting satellite (Key, 1995; 2000; Key and Intrieri, 2000). The AVHRR has five channels centered at approximately 0.6, 0.9, 3.7, 11, and 12 μm (channels 1 through 5, respectively). Global Area Coverage (GAC) data acquired from overpasses nearest to 1400 local solar time (2400 UTC) were re-gridded to a five kilometer pixel size. Calibration of channels 1 and 2 is done according to Rao (1993), which corrects for sensor drift over time. The standard NOAA/NESDIS method (NOAA, 1991) is used for the calibration of the thermal channels (channels 3, 4, and 5), with an additional correction for non-linearity. Channels 1 and 2 were further adjusted for Earth-Sun distance. The absolute accuracy of reflectance is on the order of 5–7% (Rao, 1993). The thermal channels have a radiometric accuracy of approximately 0.2 K.

2.3 NOAA Doppler radar and MWR observations

The new millimeter-wave cloud radar (MMCR) has been designed to provide detailed, long-term observations of non-precipitating and weakly precipitating clouds. Detailed information on the NOAA MMCR can be found in Moran et al (1998) and it is briefly described here. The innovative radar design features a vertically pointing Doppler system operating at 8.66 mm (35 GHz, Ka band). It uses a low-peak-power transmitter for long-term reliability and high-gain antenna and pulse-compressed waveforms to maximize sensitivity and resolution. During the SHEBA experiment, the MMCR collected data in 45 m range gates, with 9-s averaging periods between the surface and 15 km AGL. The radar was housed in a sea container, about 25 feet from the lidar. The range resolution is 45 m and a maximum range coverage of 16 km was used at SHEBA with a beam width of 0.2 degrees. The radar uses the same kind of signal processor as that used in commercial wind profilers. Attenuation by cloud liquid water content (LWC) and water vapor is negligible for the types of values encountered in the Arctic. The uncertainty in the radar derived reflectivity factor and Doppler velocity are approximately 10% and 15%, respectively. The true sensitivity of the radar measurements is about -49 dBZ at a 5 km range.

The microwave radiometer measurements at SHEBA site was made with Radiometrics WVR-1100 at 23.8 and 31.4 GHz. Brightness T at these channels were used to estimate integrated water vapor and LWP at two minutes intervals. LWP differences obtained from various MWR can be about 20% at $-10\,°C$ and details on this can be found in Shupe et al (2002).

2.4 NOAA lidar observations

The lidar system used at the SHEBA ship was the Depolarization and Backscatter Unattended

Lidar (DABUL) which was developed at NOAA's Environmental Technology Laboratory (ETL). DABUL is an active remote sensing system that transmits very short pulses of laser light at a green wavelength (0.523 μm) into the atmosphere. The energy scattered back to the system yields range-resolved information on the horizontal (from scanning data) and vertical structure of clouds and aerosols. The depolarization capabilities of the instrument provide additional information on the phase of clouds and precipitation. DABUL was designed to be fully eye-safe and to operate semi-autonomously in any environment, obtaining continuous profiles of backscatter and depolarization ratio (Alvarez et al, 1998).

Data retrieved from the DABUL system were processed to extract information about Arctic cloud heights and their phases (Intrieri et al, 2001). After the necessary corrections (i.e., background, range, and overlapping) are applied to the data, the intensity and/or depolarization ratio fields can be thresholded against a value to determine cloud base and top heights for as many layers of cloud that are detected. Once the cloud layer heights were determined, the signal-weighted average values of the depolarization ratio for each layer were calculated. These ratios yield the associated phase of that layer. The lidar was tilted 5 degree from the vertical to prevent ambiguous depolarization signatures and data were collected at 5 s intervals with 30 m resolution between the surface and 20 km AGL.

2.5 MSC lidar observations

In this study, an airborne simultaneous upward/downward looking depolarized lidar operating at 1.064 μm was used to specify the cloud top and base heights, dynamical characteristics (e.g., cells), and particle shape. The horizontal resolution using the aircraft speed is estimated to be approximately 85–100 m for 1 Hz data and the vertical resolution is about 4 m. A description of the lidar and its observations can be found in Strawbridge and Harwood (1998). The backscatter ratio (B) obtained from the lidar measurements had an uncertainty of approximately 10%. The depolarization ratio (d) is defined as the ratio of the return polarized perpendicular signal to the return polarized parallel signal (Spinhirne and Hart, 1990). The depolarization ratio was only available for the 28 April case.

3. Synoptic conditions

Large-scale cloud systems were characterized mainly by the Canadian Meteorological Center (CMC) Global Environmental Multi-scale (GEM) model and satellite observations. Airmass origin was obtained using the CMC GEM model (Cote et al, 1998; Gultepe and Isaac, 2002). The horizontal resolution over the whole domain was 15 km, and the vertical resolution was ~50 mb. Table 2 shows the cloud base and top heights (temperatures), heights of liquid cloud segments, airmass origin, range of vertical air velocity fluctuations, large-scale

Table 2. Cloud and large-scale system characteristics during flights made over SHEBA ship. The w' is vertical air velocity fluctuations, T the temperature, and z the height

Cases	Cloud top Z [km]; T [°C]	Cloud base Z [km]; T [°C]	Liquid level z [km]; T [°C]	Airmass origin	w' [m s^{-1}] interval	Synoptic system	dT/dZ and inversion base height
April 16	8.0; −42	0.1; −5.0	0.1; −5.0	Pacific	±0.8	Low-pressure system at south; weak short wave	12 °C/0.5 km 0.3 km
April 17	0.5; −5	0.15; −8.0	0.15; −8.0	Pacific	±0.5	Small weather feature	7 °C/0.2 km 0.4 km
April 21	5.0; −23	0.1; −17.5	0.2; −17.5	Pacific	±1.0	Weak trough and Upper short wave	10 °C/0.7 km 0.4 km
April 28	7.1; −43	0.1; −25	No water Droplets	Arctic	±1.1	Upper air low and trough	5 °C/0.5 km 0.1 km

system feature, and inversion base height and thermal gradient at the inversion that are obtained from the observations and model results. This table shows that cloud particles were all ice on 28 April, while they were mostly mixed phase for the lower portions of the clouds in the other cases. Phase discrimination was obtained based on aircraft optical and hot-wire probes described in the observations section. The vertical air velocity fluctuations (w′) of about $\pm 1.0\,\mathrm{m\,s^{-1}}$ at the lowest legs for 21 and 28 cases (Table 2) were larger than ± 0.5–$0.8\,\mathrm{m\,s^{-1}}$ for the other cases.

The following subsections explain the large scale atmospheric conditions and in-situ profiles during flight missions for four cases. The leads in the proximity of ship were only observed during April 28 case.

3.1 16 April case

On this day, at 12:30 UTC, a cloud layer was between the surface and 3.6 km with a solid overcast, and some liquid water at about 1.4 km height was detected by the ship-based radar and the lidar. Surface winds were from 27 degrees (0 degree representing north) at 3–$5\,\mathrm{m\,s^{-1}}$. Clouds were also seen above the boundary layer. The NOAA AVHRR image indicated that a low-pressure system was located over the southwest of the ice camp. The airmass origin was from the Pacific Ocean. An ECMWF model run indicated a weak low to the west of Barrow, moving towards the ice camp. The upper air pattern showed a weak short-wave moving over the camp. In general, rising heights correlated with a broken-cloud cover in the middle to high levels. The same system in the west affected the ice camp during the aircraft mission.

The measurements obtained during an aircraft descent are shown in Fig. 2a–e. The inversion base height was at 0.3 km on this day. Surface T was about $-10\,^{\circ}\mathrm{C}$. T gradient was $12\,^{\circ}\mathrm{C}/0.5\,\mathrm{km}$ at the inversion layer. RH_i was about 100% at low levels over the ship ($q_v \sim 1.5\,\mathrm{g\,kg^{-1}}$), and above 3 km it was slightly under-saturated. The U_h decreased from about $10\,\mathrm{m\,s^{-1}}$ at the surface to $5\,\mathrm{m\,s^{-1}}$ at 500 m. Then, it increased gradually above the 500 m level. Wind shear was $5\,\mathrm{m\,s^{-1}}/0.5\,\mathrm{km}$ below 500 m. Wind direction was from the northeast at the surface but it was from the south above 1 km height.

3.2 17 April case

For this day, the surface T was about $-8\,^{\circ}\mathrm{C}$ at 1300 UTC. Two cloud layers were indicated by the ship-based radar observations; the low layer was below 800 m and the high layer was between 1200 and 2100 m. The lower cloud layer consisted of water, and the upper cloud deck was mostly ice. Lidar returns were attenuated by the low cloud layer. Analysis of surface maps and model runs indicated that a patch of cloud containing some snow was passing over the ice camp. It was a small weather feature, and it was moving north of the ice camp.

The measurements obtained during an aircraft ascent are shown in Fig. 2f–j. The inversion base height was at 0.4 km. Surface T was about $-10\,^{\circ}\mathrm{C}$ and T gradient was $7\,^{\circ}\mathrm{C}/0.2\,\mathrm{km}$ at the inversion layer. The uncertainty in in-situ T is about 1–2 °C, and that can explain the difference between aircraft and ship-based measured temperatures. RH_i was about 100% at low levels over the ship ($q_v \sim 2.0\,\mathrm{g\,kg^{-1}}$), and above 0.5 km it was completely under-saturated. The U_h decreased from about $10\,\mathrm{m\,s^{-1}}$ at 700 m down to $2\,\mathrm{m\,s^{-1}}$ at 200 m. It increased gradually from $10\,\mathrm{m\,s^{-1}}$ (700 m) to about $30\,\mathrm{m\,s^{-1}}$ at higher levels.

3.3 21 April case

For this day, the surface T in the ice camp was about $-18\,^{\circ}\mathrm{C}$. The inversion height was about 500 m at 0000 UTC. Winds were about $10\,\mathrm{m\,s^{-1}}$ from NE. The rawinsonde sounding at 2315 UTC (not shown) indicated that clouds were possibly between 950 mb and 1000 mb. Some low and mid-level clouds were also present. The airmass origin was from the Pacific region. A broken cloud field moving north towards the camp was seen on the satellite images. Two weather features dominated the ice camp. The first feature was a surface high that moved over ice camp from the east, covering a very large area. The second feature was a small short-wave in the upper air flow. There was a weak trough over the camp which was likely the reason for the mid-level clouds over the camp.

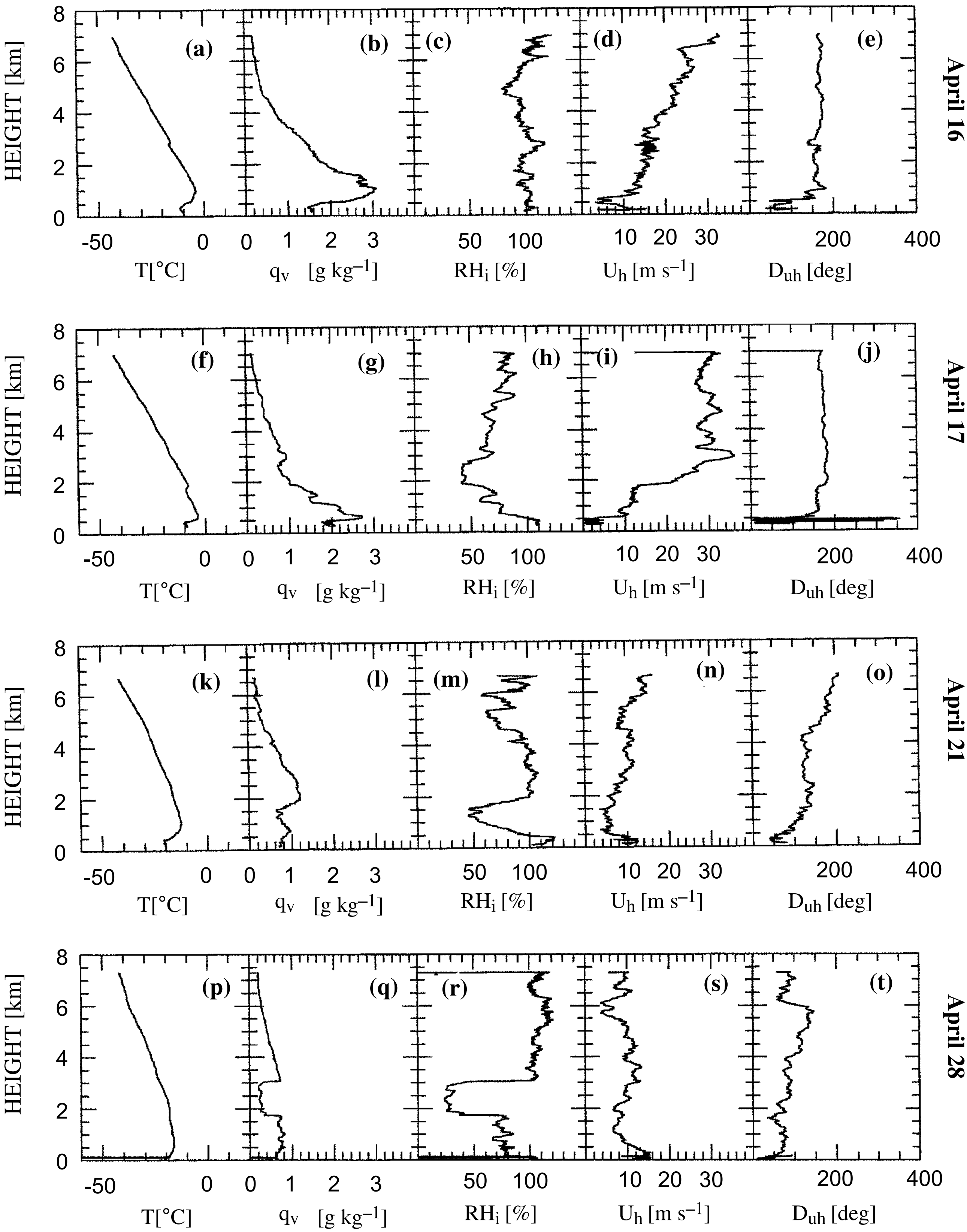

Fig. 2. Profiles of aircraft measurements for all cases made nearby the SHEBA ship. Temperature, vapor mixing ratio, relative humidity with respect to ice, horizontal wind speed, and direction are shown by T, q_v, RH_i, U_h, and D_{uh}, respectively. Sharp changes in wind measurements should be considered cautiously

The measurements collected during the aircraft ascent are shown in Fig. 2k–o. The inversion base height was at 0.5 km on this day. Surface T was about $-20\,°C$ and T gradient was $10\,°C/0.7$ km at the inversion layer. RH_i was larger than 100% at low levels over the ship ($q_v \sim 1.0\,g\,kg^{-1}$), and above 0.5 km it was very dry. The RH_i was about 100% again at about 2 km. The U_h decreased from about $10\,m\,s^{-1}$ at the surface to $5\,m\,s^{-1}$ at 500 m, similar to other cases. It stayed constant up to 1.5 km, and then started to increase. Wind shear was $5\,m\,s^{-1}/0.5$ km below 500 m. Wind direction changed from northwest at the surface to south at high levels.

3.4 28 April case

For this day, T at the surface was about $-18\,°C$ at 1300 UTC, and winds were at $13\,m\,s^{-1}$ from 65 degrees. There was refrozen lead activity on this day. Large cloud systems were in the southern part of the Arctic Ocean. Mid-level clouds were seen at 1500 UTC. The rawinsonde sounding at 2325 UTC indicated that cloud activity was minimal but broken clouds were seen at all levels. High-level clouds above 650 mb were also present. NOAA AVHRR IR images showed a cloud mass mainly to the west of the ice camp. Ice patterns at the surface were visible in the north and east of the camp indicating a weak or non-existing boundary layer cloud. Winds shifted to the north at the ice camp and increased slightly. Cloud cover increased slowly during the day as the low moved into the Arctic from Northern Alaska. The main upper air low and trough were southeast of the ice camp. Back trajectory analysis indicated that the airmass originated from the Arctic Ocean. Pinto et al (2001) indicated that a lead started to be refrozen on this day, resulting in small heat and moisture fluxes, where air parcels never reached a condensation level.

For this day, measurements collected during an aircraft descent are shown in Fig. 2p–t. Profile values on this day were very different as compared to the other cases. The inversion base height was at 0.1 km and surface T was about $-20\,°C$. T gradient was about $5\,°C/0.5$ km at the inversion layer. RH_i was larger than 100% at very low levels over the ship ($q_v \sim 0.6\,g\,kg^{-1}$), and above 0.2 km, RH_i was about 75%. Between 2 and 3 km heights, RH_i was less than 50%, and above 3 km, the air became saturated again. The U_h decreased from about $15\,m\,s^{-1}$ at the surface to $5\,m\,s^{-1}$ at 1 km. Then, it fluctuated between $5\,m\,s^{-1}$ and $10\,m\,s^{-1}$ at higher levels. Wind shear was $10\,m\,s^{-1}/1$ km below 1 km. Wind direction changed from northeast at the surface to east at high levels.

4. Method

In this section, the calculation of microphysical and dynamical parameters from aircraft observations, and retrievals of some microphysical parameters, e.g. effective size and IWC (LWC) from Doppler radar, MWR and satellite observations are explained. Because of the advection of cloud systems over the region, satellite observations from an area of $50\,km^2$ were used in the comparisons. Note that the SHEBA ship location on the 28 April case was significantly away from the aircraft flight segments.

4.1 Calculation of cell sizes and turbulent heat fluxes

The sizes of the cells were defined using a criterion that is based on the mean and standard deviation (sd) of the reflectivity from Doppler radar observations, backscatter ratio from lidar, and vertical air velocity fluctuations (w') from the aircraft observations. On a cloud scale (e.g., >10 km), w' can be approximately equal to the measured w when the mean vertical air velocity is assumed to be small as compared to observed values. When a measurement was found larger than the mean plus sd, it was used as an indication of cells. Note that this definition doesn't include the temperature parameter that is important for convective cell definition. Also, the cell definition here should not be related to deep convective systems.

An eddy correlation technique similar to Smith and MacPherson (1996), and Gultepe and Starr (1995) is used to obtain SHF and LHF fluxes. In the flux calculations, the Li-Cor data was advanced 1.4 seconds relative to the vertical gust velocity to account for instrument response and the longitudinal displacement between the gust boom and the analyzer. The vertical air velocity, potential temperature, and mixing ratio fluctuations along 30 km-long constant altitude flight legs at about 150 m height are used in the calculations. A description of how wind measurements are obtained from the Convair-580 and their accuracy can be found in Williams and Marcotte (1999), and Gultepe et al (2003). They stated that, under the steady flight conditions, the corrections to wind measurements were found to be negligible. Turbulent flux calculations from Convair-580 data were also used in the studies of Curry et al (2000), and Smith and MacPherson (1996).

4.2 Calculation of cloud microphysical parameters

Ice crystal effective radius (r_{effi}) is an important parameter for climate change studies. The r_{effi} is estimated using an equation given by Francis (1995) as

$$r_{effi} = \frac{3}{4\rho_i}\frac{IWC}{\sum_i n_i A_i}, \tag{1}$$

where IWC is in [$g\,m^{-3}$], ρ_i the ice crystal density, A the cross sectional area [m^2], and n_i number concentration [m^{-3}] where i represents bin size. For droplets, r_{eff} is obtained as the ratio of the 3rd moment of particle distribution to the 2nd moment (Gultepe et al, 2001b). Equation (1) is also used to estimate retrievals of ice microphysical parameters from AVHRR observations (Key et al, 2001). As explained earlier, the water and ice regions were separated using the Rosemount ice detector and other microphysical probes (Cober et al, 2000; Gultepe et al, 2001a). Ice microphysical characteristics (e.g., particle shape and size) were obtained using geometrical ratios defined in Heymsfield and Parrish (1978). The IWC calculation from the PMS 2D-C probe can have an uncertainty of around 20–50% due to unknown particle shape and concentrations at small and large particle channels.

4.3 Microphysical retrievals from NOAA/ETL Ka-band radar observations

Using an assumption of spherical particles, retrievals of ice microphysical characteristics including IWC, and r_{effi} for the 28 April case (with no LWC) are obtained using a method given by Matrosov (1998; 1999) that utilize the measurements of both an IR radiometer and ETL Ka-band (35 GHz) radar. In this method, "tuned coefficients" based on observed radar reflectivity and radiometer measurements were used (Shuppe et al, 2002; Matrosov et al, 1999). The final equations to obtain IWC and r_{effi} are given by Shupe et al (2002) as

$$IWC = aZ_e^b, \tag{2}$$

and

$$r_{effi} = 0.14\left(\frac{Z_e}{74\times10^{-6}\,IWC}\right)^{1/1.9}, \tag{3}$$

respectively, where a and b are tuned parameters, having a constant value within the cloud ($IWP/Z_e^{b(h)}\Delta h$) and ranging from 0.7 at the cloud base to 0.6 at the cloud top, respectively. The Δh is the layer thickness where reflectivity is averaged. $Z_e[mm^6\ m^{-3}] = 0.2Z_i = 10^{(Z[dBZ]/10)}$. In the preceding equation, Z_i is the reflectivity for ice crystals. Relative standard deviations of retrieved size and IWC from in-situ measurements can be up to 30 and 55%, respectively (Matrosov et al, 1999).

For the 16 and 21 April cases (with presence of LWC), IWC and r_{effi} are obtained using the Doppler radar technique (Matrosov et al, 2002). In this technique, the mean vertical air velocity over approximately a 20 km length scale is assumed to be negligible. Then, $V_r \approx V_z$ where V_z is the reflectivity weighted cloud particle fall velocity obtained from Doppler radar measurements. The median diameter D_o, then, is obtained from the following equation:

$$V_z = Aa_1D_o^B, \tag{4}$$

where a_1 is a coefficient dependent on the particle size distribution. The A and B are the coefficients in the relationships between particle size and terminal velocity and $B \approx 0.17A^{0.24}$ (Matrosov and Heymsfield, 2000). They showed that a new coefficient (G) dependent on particle shape, size, and density, IWC is obtained as

$$IWC = Z_e/GD_o^3. \tag{5}$$

4.4 Retrievals from NOAA AVHRR observations

Cloud detection utilizes reflectance at 0.9 and 3.7 μm as well as the difference in brightness temperatures at 11 and 12 μm. Reflectance at 3.7 μm, which also contain an emitted thermal component, were approximated by removing an estimate of the emitted portion based on the temperature at 11 μm from the total radiance:

$$\rho_3 = \frac{L_3 - B_3(T_4)}{L_0\mu - B_3(T_4)}, \tag{6}$$

where ρ_3 is the channel 3 reflectance, L_3 the channel 3 radiance, $B_3(T_4)$ the Planck function for channel 3 based on the channel 4 temperature T_4, L_0 the solar constant for the band (adjusted for Earth-Sun distance), and μ the cosine of the solar zenith angle. Equation (3) is derived from the following basic relationship:

$$L_3 = (1 - \rho_3)B_3(T_4) + \rho_3 L_0\mu, \tag{7}$$

where $1 - \rho_3$ is the emissivity. This relationship assumes that the surface or cloud in the field-of-view does not transmit any radiation, and that emission and reflection are isotropic. Without any prior knowledge of the scene, these assumptions are necessary. Roger and Vermote (1998) presented an alternative method of estimating the 3.7 μm reflectance where the channel 3 thermal radiance was parameterized as a function of the channels 4 and 5 brightness temperature difference in nighttime imagery. While this may be a more realistic approach, Xiong et al (2002) found that the difference between the two methods in estimating the thermal radiance for an Arctic case study was less than 5%. During the daytime, cloud detection is accomplished with spectral threshold tests, as described in Key (2000).

All clouds considered here are assumed to be composed of either liquid droplets (''water cloud'') or ice crystals (''ice cloud''). No attempt was made to identify mixed-phase or multi-layer clouds. The determination of cloud particle thermodynamic phase was based on both physical and spectral properties. Physically, liquid cloud droplets can exist at temperatures as low as −40 °C, although clouds are likely to be composed of both liquid droplets and ice crystals at temperatures below −10 °C. The spectral difference between water and ice clouds occurs because of differences in absorption and scattering. The phase detection algorithm relies on differences in the single scattering albedo of water and ice clouds at 3.7 μm, and differences in the imaginary index of refraction which gives rise to brightness temperature differences at 3.7 (night), 11, and 12 μm. Key and Intrieri (2000) described the physical principles and algorithm in detail.

Cloud optical depth retrievals are done using a comprehensive database of modeled reflectances and brightness temperatures covering a wide range of surface and atmospheric conditions. The basic approach for daytime retrievals of water cloud follows that of Nakajima and King (1990), who showed that reflectances at absorbing wavelengths (e.g., 3.7 μm) are primarily dependent upon particle size while reflectances at non-absorbing wavelengths (e.g., 0.6 or 0.9 μm) are more a function of optical depth. Reflectances were modeled with Streamer (Key and Schweiger, 1998), which utilized a discrete-ordinates solver, parameterized cloud and aerosol optical properties, and gaseous absorption. Water cloud optical properties are based on Mie theory. Ice cloud optical properties are from Fu and Liou (1993), who developed a parameterization based on geometric ray-tracing of scattering by randomly oriented hexagonal crystals for a size parameter (analogous to effective radius) greater than 30 μm and the exact spheroid solution for size parameters less than 30 μm. Fu and Liou (1993) made their calculations based on aircraft observations, using 11 size distributions covering ice water contents from 6.6×10^{-4} to $0.11\,g\,m^{-3}$, and mean effective sizes from 23.9 to 123.6 μm. The spectral bands in their study that, correspond to the AVHRR channels, are 0.7–1.3 and 3.5–4.0 μm.

For ice clouds, the 3.7 μm reflectance for the daytime is so small that it is unreliable. Therefore, 11 and 12 μm brightness temperatures were used to obtain a range of possible solutions and the 0.9 μm reflectance was used to constrain the solution. Brightness temperature differences were also used to constrain the solution for thin water clouds over snow, when the solution based on reflectance alone may not be unique. These procedures are detailed in the Key (1995; 2000) studies.

5. Results

In this section, the results related to microphysical and dynamical characteristics of the Arctic clouds are summarized based on the observations obtained from the aircraft and remote sensing platforms.

5.1 In-situ observations

5.1.1 Aircraft profiles

Profiles of observations obtained from the aircraft instruments are shown in Fig. 2 and the synoptic conditions related to these profiles have been described in Sect. 3. As a brief summary, the winds were northerly or northeasterly at the surface, except for the 17 April case. At high levels, winds were generally southerly, except for the 28 April when they were northeasterly and easterly. In general, the low levels were saturated with respect to ice. An inversion layer at about 0.1 km occurred for all cases. Stronger wind shear in a deep layer was seen for 16 and 17 April cases as compared to the other two cases. In fact, low-level wind shear in the vertical was always present.

5.1.2 SHF, LHF, θ', q_v' and w' time series

The time series of radiance from the LANDSAT simulator (R_{ch1}) at relative units, vertical air velocity, potential temperature, and water vapor density fluctuations (w', θ', and q_v', respectively), SHF, and LHF were obtained for each case over approximately a 30 km scale near the SHEBA ship.

Figure 3 shows the above parameters obtained at constant altitude flights at about 150 m nearby the ship. The airborne LANDSAT simulator (also PRT-5 IR radiometer, not shown) data show that leads were present only on the 28 April case. The w' magnitude was smaller for the 17 April case as compared to the other cases (Table 2). The maximum w' was observed for the 28 April case where leads were observed. When the aircraft flew over the ship at about 2350 UTC, the leads had started to re-freeze (Pinto et al, 1999). Dynamical structures were observed from the scales of 3 m up to 10 km for all cases. Overall, LHF and SHF were found to be less than 75 and 200 W m^{-2}, respectively. Large portions of these fluxes are thought not to be related to surface conditions, but likely generated by some in-cloud processes.

The ice crystal number concentration (N_i) versus w ($w' \sim w_{obs} \sim w$, and mean $w \ll w_{obs}$) relationship is important for modelers who study cloud development (Clarke et al, 1999; Gultepe et al, 2000). For this reason, N_i obtained from the total number of strobes is plotted versus w after the means are removed for each case (Fig. 4). This figure shows that the maximum N_i reaches 300 l^{-1} when w is near 0 m s^{-1}. It decreases generally when w fluctuates away from zero. For the 17 April case, N_i reached 500 l^{-1} with w' between -1.5 and $+1.5$ m s^{-1}. For the 21 April case, N_i reached 500 l^{-1} when w' was between -1 and 1 m s^{-1}. For the 28 April case, N_i was about 200 l^{-1} for the same interval. Figure 4 shows two important results: (1) large values of w' result in smaller N_i, and (2) low values of w can result in various peak N_i values that are likely dependent on supersaturation with respect to ice (S_i), N_a, and T (Gultepe et al, 2001a). Note that the mean w from aircraft data is not accurate enough to make any conclusions about large-scale w. Large values of N_i also indicate the existence or past experience of updraft by the air parcel, or the air parcel from which the large ice crystals fall out. When eddies and turbulent motions over various scales are present, particles collide and become larger, resulting in a decrease in N_i that is seen in related figures. It is well known that increased mean w results in an increased N_i as theory suggests (Jensen et al, 1994). They found that N_i increases with increasing w as a result of cooling processes. Note that N_i in Fig. 4 is obtained from the PMS 2D-C probe total strobe counts, and no filtering is applied to the observations. N_i must be considered as a qualitative number because particles less than 100 μm are counted with an unknown but highly reduced efficiency and very small particles are not counted at all. Gultepe et al (2001a) showed that 2D-C measurements can be about 2–5% of N_i obtained from FSSP measurements at small size ranges. In order to directly compare 1 Hz w data with ice particle concentrations, it is necessary to use the total strobe approximation for ice particle concentration.

5.1.3 Liquid microphysical characteristics

In this section, the mean and sd of LWC, r_{eff}, TWC, w fluctuations, and N_d averaged over a

30 km scale within the cloud are summarized for each case shown in Table 3. LWC regions are segregated from ice regions using the Rosemount ice detector and hot-wire probe measurements as explained earlier. The large TWC for the 17 April case is likely related to the embedded small-scale convective processes occurring within the large-scale systems. The mean values of r_{eff} are about 1 μm higher for the larger size range FSSP probe on the 16 and 21 April cases, indicating the possibility of relatively large droplets being present on the 16 and 21 April cases. N_d for the 17 April case is about 2 times larger than that of other cases, which can possibly be explained by the higher N_a value observed on this day. Note that there was no liquid within the observed clouds on the 28 April case.

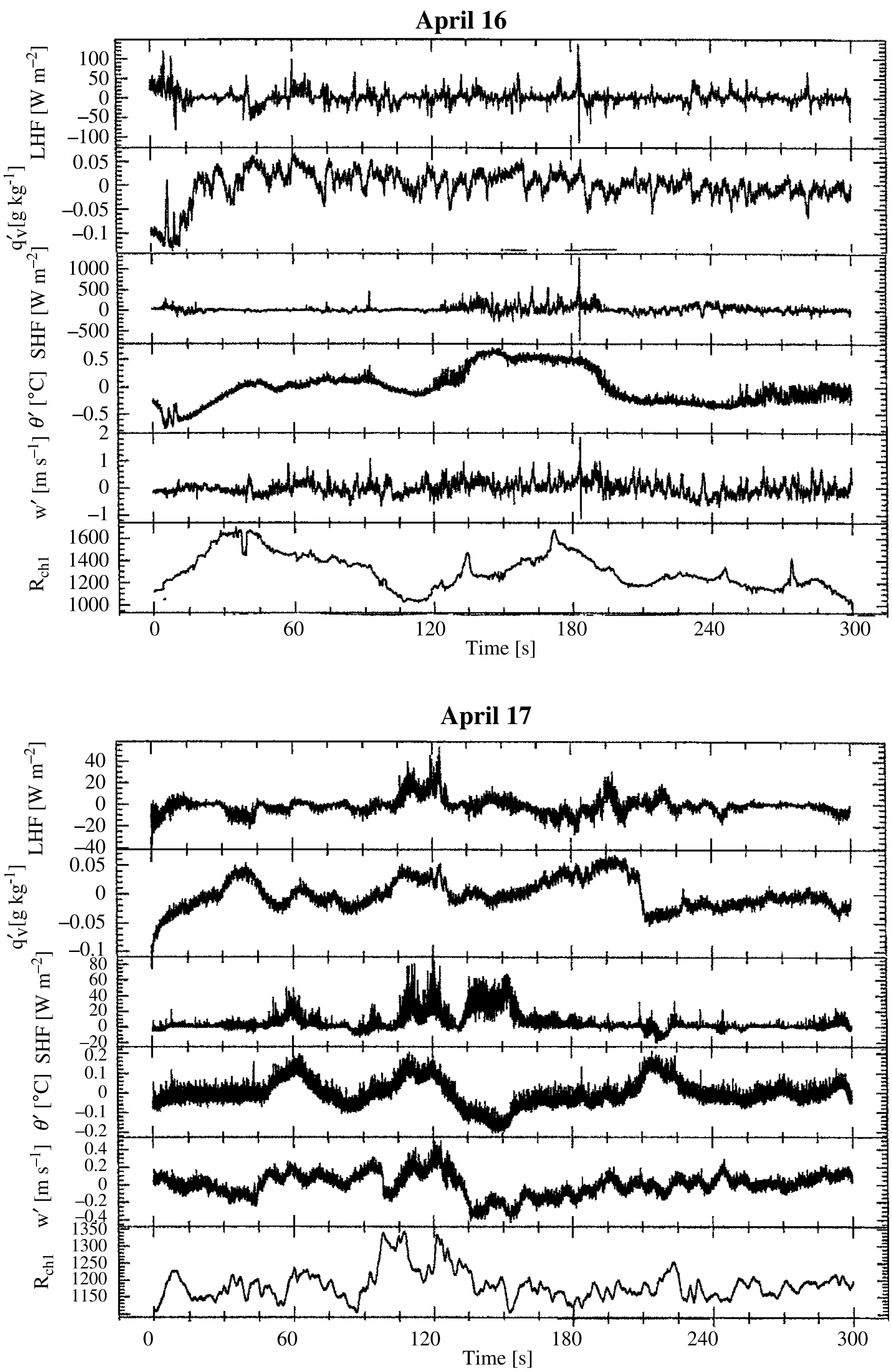

Fig. 3. Time series of LANDSAT simulator radiance at relative numbers, vertical air velocity, potential temperature, and vapor mixing ratio fluctuations, sensible heat fluxes (SHF) and latent heat fluxes (LHF) over the lowest constant altitude flights (∼ km) for four cases

April 21

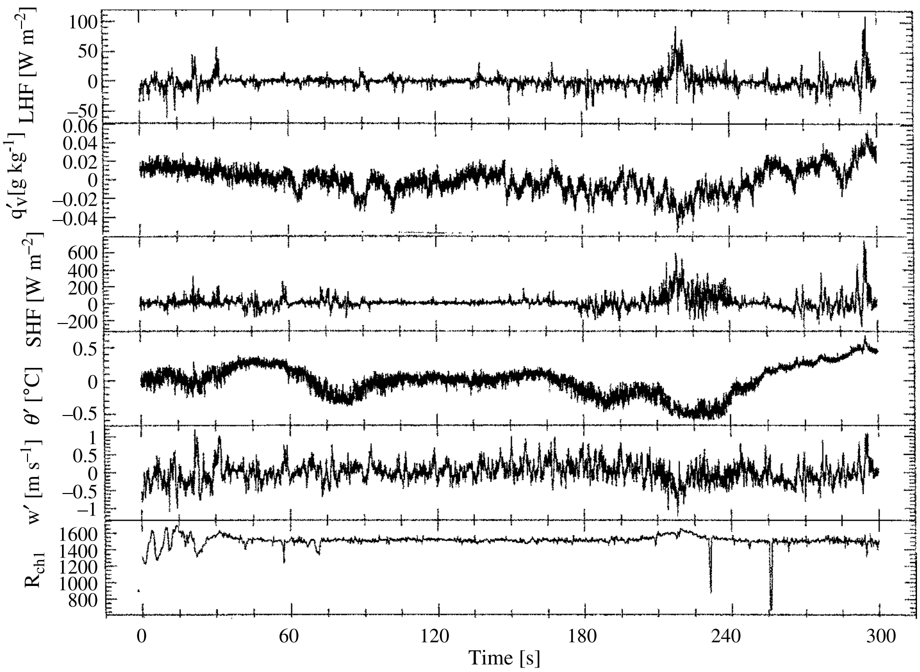

April 28

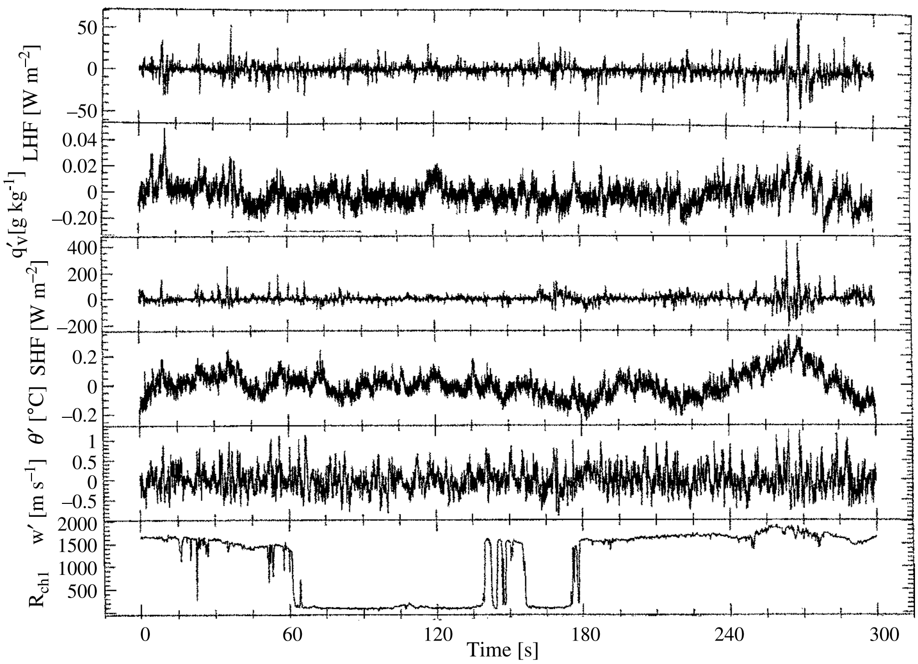

Fig. 3 (*continued*)

Cross correlations among microphysical parameters are shown in Fig. 5. For the 16 April case, r_{eff} had approximately a linear relationship with LWC (box a). The r_{eff} for the 17 April case was almost constant ($\sim$10 µm). For the 21 April case, it increases exponentially with increasing LWC and its values are less than 8 µm. This value is likely a result of a polluted airmass effect that was indicated by Gultepe and Isaac (2002). In general, r_{eff} values are less than 12 µm for all cases. A LWC versus N_d relationship was only found for the 17 April case (box b), but the number of data points was not distributed equally. The r_{eff} decreased with increasing N_d for the 17 and 21 April cases (box c). The other cases did not show a clear relationship.

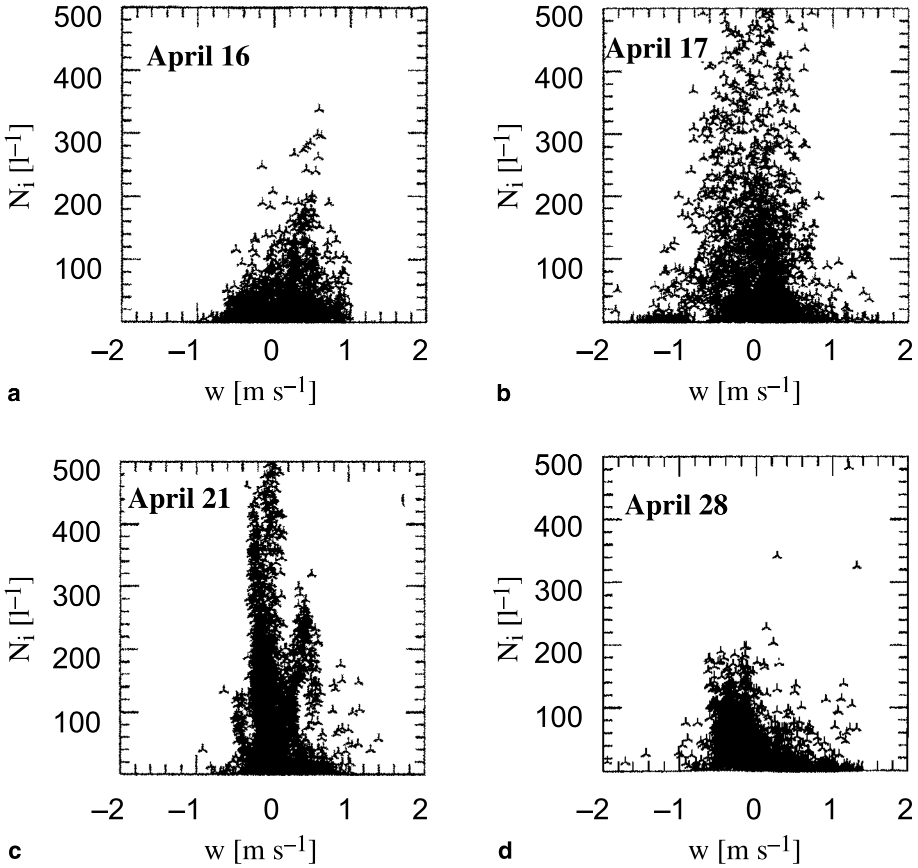

Fig. 4. Vertical air velocity fluctuations versus ice crystal number concentration for all cases. Mean w is taken out of the time series

Table 3. The 300-s average and sd values of parameters over the constant altitude flight leg segments. The z, T, q_v, r_{eff96}, LWC_{96}, N_{d96}, r_{eff124}, LWC_{124}, N_{d124}, LWC_k and N_a, are height, temperature, vapor mixing ratio, effective radius, liquid water content, and droplet number concentration for the FSSP-96 and FSSP124 probes, liquid water content for King probe, and aerosol number concentration, respectively. Subscripts 96 and 124 represent two size ranges of the FSSP-100

Days → Parameters ↓	April 16	April 17	April 21	April 28
Z [km]	0.06 ± 0.05	0.15 ± 0.03	0.19 ± 0.07	0.05 ± 0.01
T [°C]	-9.5 ± 3.9	-9.6 ± 0.6	-21 ± 0.42	-20.3 ± 0.27
q_v [$g\,kg^{-1}$]	3.2 ± 0.1	2.45 ± 0.14	1.00 ± 0.03	0.91 ± 0.03
r_{eff96} [μm]	9.3 ± 3.0	9.9 ± 0.8	6.3 ± 6.1	–
LWC_{96} [$g\,m^{-3}$]	0.05 ± 0.04	0.19 ± 0.04	0.02 ± 0.03	–
N_{d96} [cm^{-3}]	17 ± 11	57 ± 14	30 ± 40	–
r_{eff124} [μm]	10.4 ± 5	–	7.4 ± 7.6	–
LWC_{124} [$g\,m^{-3}$]	0.07 ± 0.06	–	0.04 ± 0.06	–
N_{d124} [cm^{-3}]	28 ± 19	–	34 ± 47	–
LWC_k [$g\,m^{-3}$]	0.06 ± 0.05	0.15 ± 0.07	0.03 ± 0.05	–
N_a [cm^{-3}]	29 ± 32	118 ± 50	68 ± 45	83 ± 16

5.2 Comparisons of ice microphysical parameters obtained from in-situ and NOAA Doppler radar measurements

NOAA Doppler radar observations were available for the all cases. The reflectivity field for the 17 April case was negligible. Cloud measured echo (reflectivity) for the 16 April case was between 100 m and 6.5 km (Fig. 6a). After 2300 UTC, the cloud had two layers; the lower layer had a maximum value of 5–10 dBZ, and the

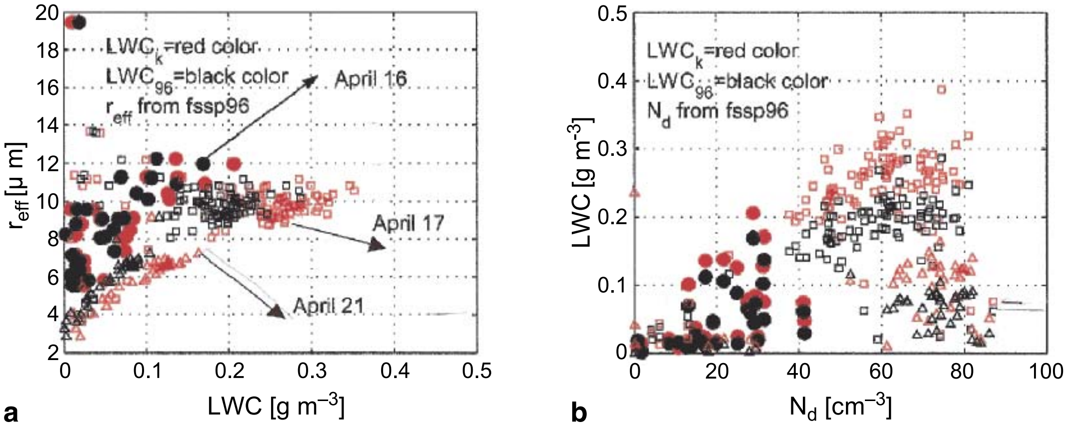

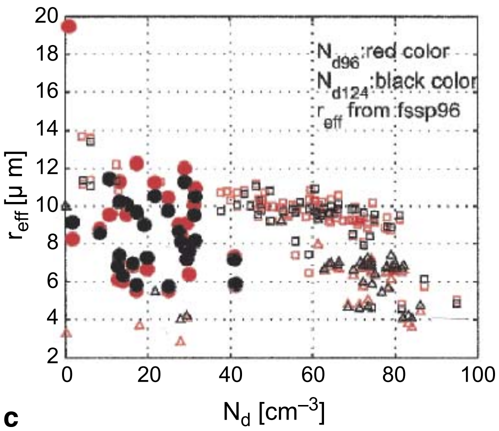

Fig. 5. Scatter plots of cloud liquid microphysical parameters for three cases. The subscript 96 and 124 represent measurements made with the PMS FSSP-96 and FSSP-124 probes, respectively. The red and black colors are for LWCk as derived from the King hot wire probe and the LWC96 calculated from the FSSP-96 probe, respectively

upper layer had a maximum of −30 dBZ. This shows that the generating region was at the top of the layer (2.5 km) where shear was observed below 1 km (not shown). The aircraft was over the ship region after 20:00 UTC when the LWP is about 20–30 g m^{-2} (Fig. 6a). Figure 6b shows radar observations for the 21 April case. After 1800 UTC, there was almost no liquid water content. Reflectivity values were between −30 and 20 dBZ and high reflectivity lines, likely due to falling particles, were evident. Aggregates of large particles are probably the source of these high reflectivity regions. Radar reflectivity on 28 April case is shown in Fig. 6c where the aircraft flew over the SHEBA site after 2100 UTC. Ze values were between −30 dBZ and 5 dBZ, and high reflectivity cores were associated with wind shear regions between 2 and 7 km that were observed by rawinsonde soundings (not shown). The MWR did not indicate liquid regions in the vicinity of the ship. The high Z_e regions with slopes for the 21 and 28 April cases (Fig. 6) indicate that wind shear was important for cloud dynamical development on these days. The wind shear can play an important role for generating eddies that contribute to the cloud development in the vertical through transferring heat and moisture to higher levels (Gultepe and Starr, 1995).

The Doppler velocity (Fig. 7) for all cases was found between a few cm s^{-1} and 1 m s^{-1} (downward), indicating that particle fall velocity was generally larger than the vertical air velocity. The smallest V_r values were observed for the 28 April case. When particles form, they start to fall, and aggregation processes significantly increase the particle size and fall speed. Note that the radar cannot usually see small particles that form at cloud tops. The radar can detect ice crystals with effective sizes larger than 8 μm and droplets with sizes larger than 3 μm. These results indicated that embedded high reflectivity cores were present for all cases except that they were relatively weak for the 28 April case. It is seen from Fig. 7 that there were significant inhomogeneities in

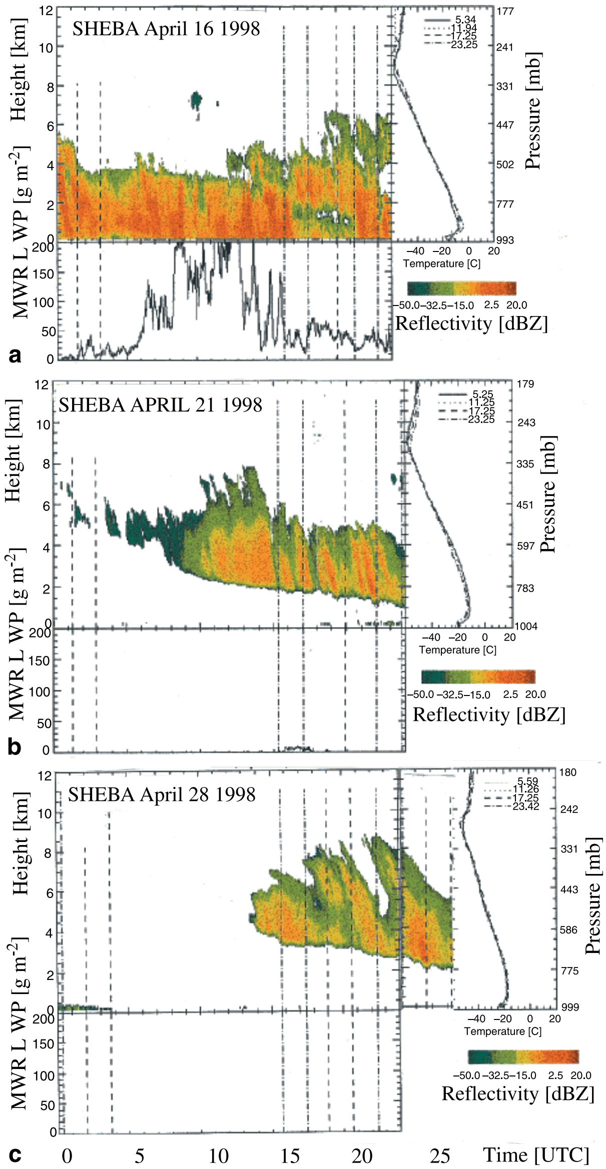

Fig. 6. Reflectivity and LWP versus time obtained from the NOAA Doppler radar and MWR observations, respectively, for three cases. The rawinsonde profiles are also shown for various time periods for each case

the V_r field that probably occurred due to dynamical activities and microphysical processes.

Ice crystal microphysical parameters, e.g., IWC, ice crystal effective radius (r_{effi}), and N_i, were obtained from the aircraft in-situ data using a similar analysis given in Francis (1995), Fu (1996), and Gultepe et al (2001a). The results are shown in Fig. 8 for all cases.

The 2DC r_{effi} for the 16 April case (Fig. 8) decreased gradually from about 70 µm close to the surface to 20 µm at about 7 km. The FSSP r_{effi} decreased from about 35 µm close to surface to 3–4 µm at the highest level. An estimate of the total N_i can be obtained by combining 2D-C and FSSP N_i measurements ($75\%N_{if} + 25\%N_{i2dc}$), based on $N_i(<100\,\mu m) \gg N_i(>100\,\mu m)$, resulted in a decrease in r_{effi}. The r_{effi} values obtained from Doppler radar observations (r_{effRR}), using the Doppler radar method (Matrosov et al, 2002), are also shown in Fig. 8. The results show that small ice particle concentration significantly affects the r_{effi} calculation although r_{effi} values are comparable at the large size-range. In general, IWC obtained from 2D-C probe decreases with increasing height but the Nevzorov probe measured larger IWC, likely due to small ice particles contribution. N_i profiles did not show a clear trend with height although some decrease occurred in N_{i2DC} at high levels. For the 17 April case, radar observations were not available but results from in-situ data are shown in Fig. 8 to compare with satellite based microphysical parameters. In this case, cloud was at the lower boundary layer ($z < 1$ km). For the 21 April case (Fig. 8), results are found similar to other cases. The r_{effi} values showed comparable results for the large particle size range ($>100\,\mu m$). Note that r_{effRR} is obtained using a particle size distribution covering the entire size range. In general, IWC values are found smaller than radar derived IWC values. This can be due to a fixed ice crystal density value. The N_i obtained from the 2D-C probe decreased with increasing height. For the 28 April case, aircraft collected data at a slightly different location, although radar did not show the cloud at low levels, the MSC lidar indicated low level clouds reaching the surface (shown in a figure given later on). The r_{eff2DC} were found to be larger compared to r_{effRR} that is likely due to use of 2D-C size range greater than 100 µm. In fact, when FSSP measurements are used, r_{effRR} and in-situ derived r_{effi} are found comparable (Fig. 8). The IWC values obtained from the TWC probe is found larger than both radar and 2D-C based values, indicating that radar derived IWC are underestimated at some levels. This can be due to the small ice crystal concentration that is evident in FSSP derived N_i values shown in Fig. 8. On this day, both FSSP and 2D-C derived N_i values increased with increasing height.

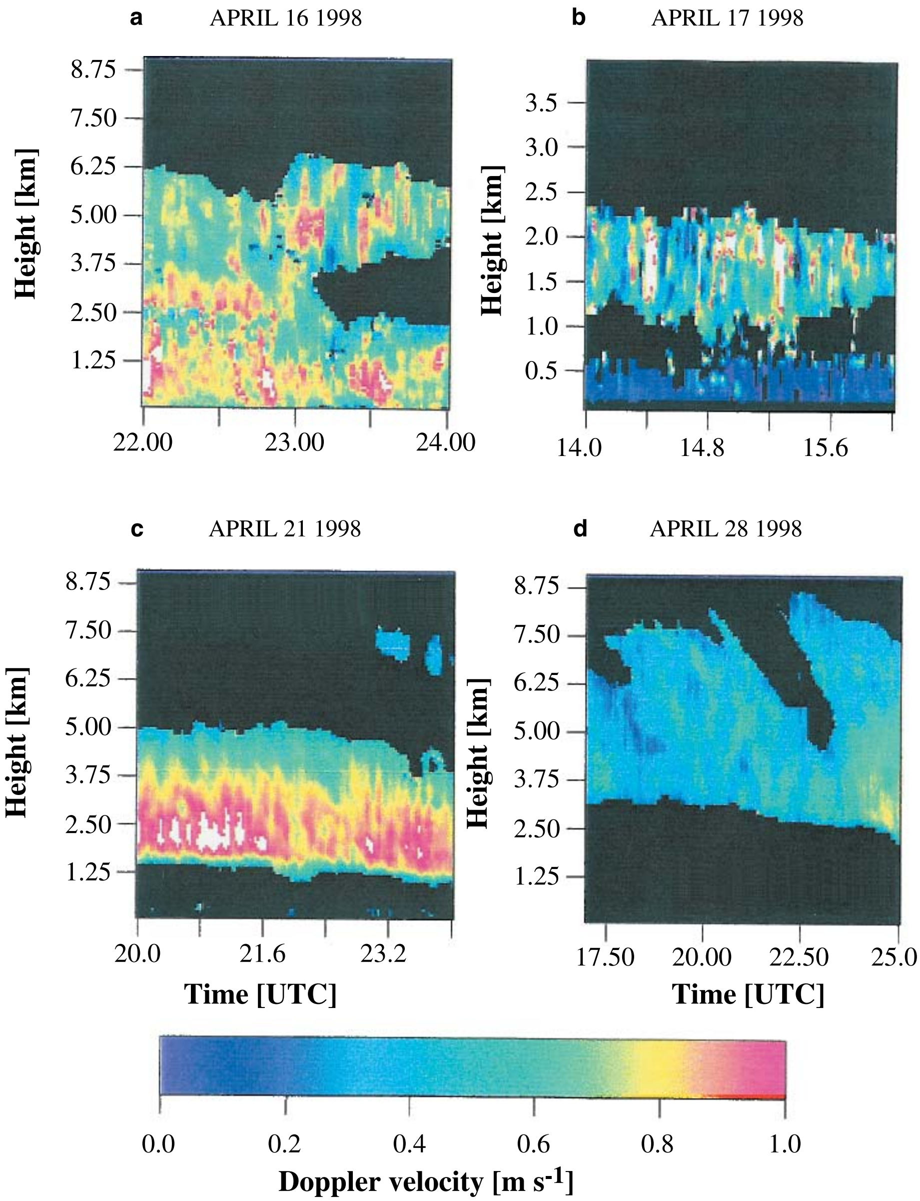

Fig. 7. Doppler velocity obtained from NOAA Doppler radar observations for all cases

5.3 NOAA AVHRR retrievals of microphysical parameters

The NOAA AVHRR observations were used to obtain effective radius, optical depth, and phase of the clouds for 3 cases (Fig. 9), excluding the 16 April case because observations were not available. The approximate location of the SHEBA ship is shown with a "X". This figure shows effective radius (left boxes) and optical thickness (right boxes) for water and ice pixels, and the large values of effective radius represent the ice region of the cloud. It is also seen in this figure that horizontal variability in the retrieved parameters is large over a small distance. The results obtained from these figures are summarized in Table 4. The table shows that r_{effi} is less than 35 µm for all cases and the smallest r_{effi} (12.1 µm) is found for the 28 April case where optical thickness is 7.8. As shown in the previous subsection, the small particle concentration can be much larger than that of large particles with sizes greater than 100 µm. Mean r_{eff} for the liquid phase for the 17 and 21 April cases are found to be approximately 10 and 8 µm, respectively, which are in close agreement with the aircraft measurements shown in Fig. 5. As with the aircraft observations, the frequency occurrence for

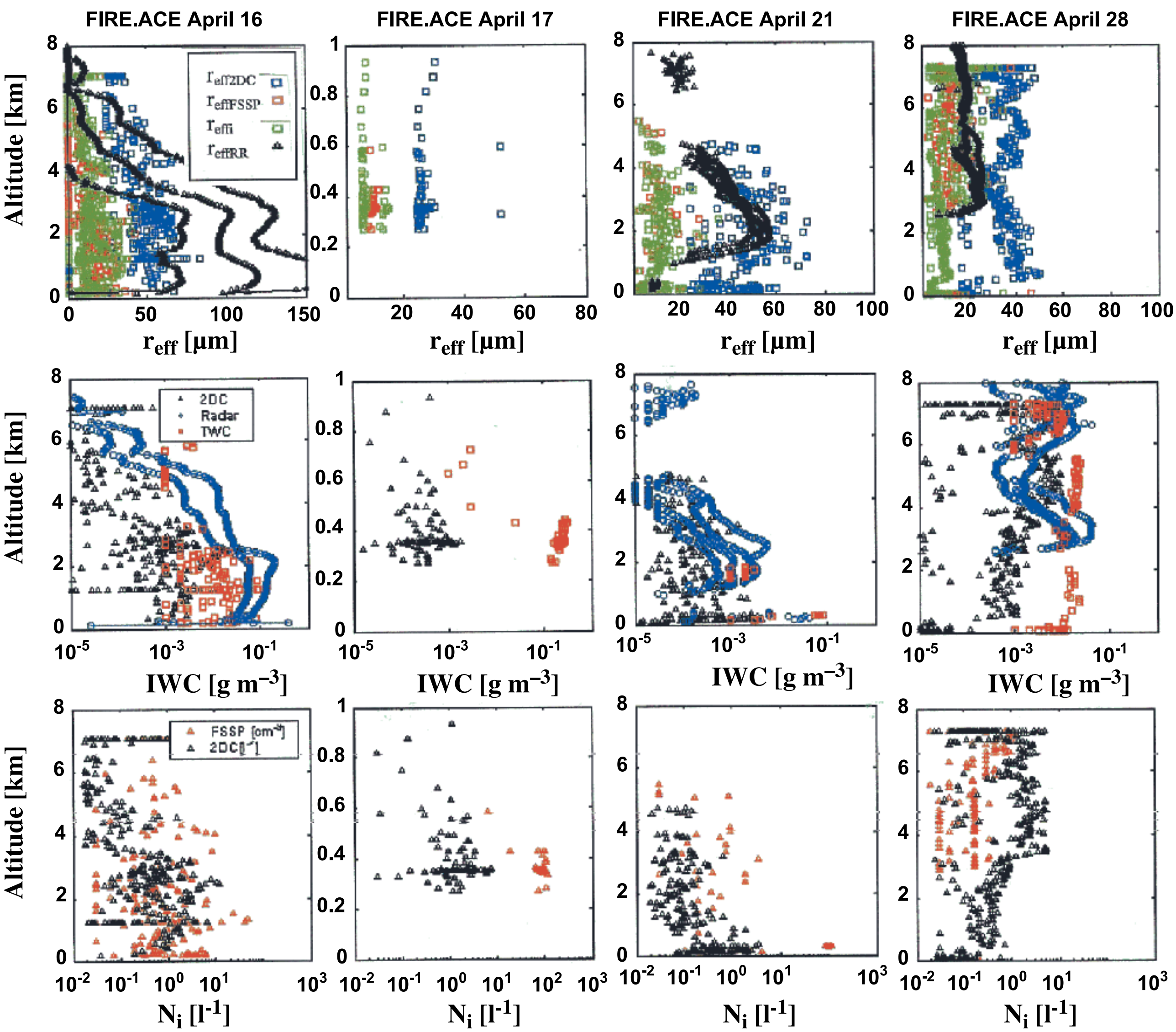

Fig. 8. Scatter plots of r_{effi}, IWC, and N_i versus height (z) for each case. Effective size is obtained from 2D-C probe measurements with sizes greater than 100 μm. FSSP based r_{eff} measurements representing sizes less than 100 μm are shown with $r_{effFSSP}$. The $r_{effFSSP} + r_{eff2DC}$ representing a total of 75% N_{if} and 0.25% N_{i2DC} is also shown. The r_{effRR} represents the radar methods; the Doppler radar method is used for both 16 and 21 April cases, and radar-radiometer method is used for 28 April case. The lines with triangles for 16 April case shows standard deviations around the mean. The triangles for 21 and 28 April cases show various profiles. For 17 April case, radar observations were not available

water to ice ratio is found to be highest for the 21 April case. The range of satellite-derived r_{effi} given in Table 4 for the 21 April is similar to the aircraft measurements shown in Fig. 8.

5.4 NOAA lidar depolarization and backscatter ratios

The depolarization ratio (d) and backscatter ratio (B) obtained from the NOAA lidar observations are shown in Fig. 10a–h for all cases. In this figure, the boxes on the left are for depolarization ratio values. For the 16 April case, high-level clouds in Fig. 10a were at about 2.5 km (pink color for liquid clouds), and low-level cloud tops, in general, were less than 1 km (Fig. 10b). Particles from high-level clouds were falling down to low levels where the streaks had large slopes. It is possible that the lidar could not penetrate above 1 km due to

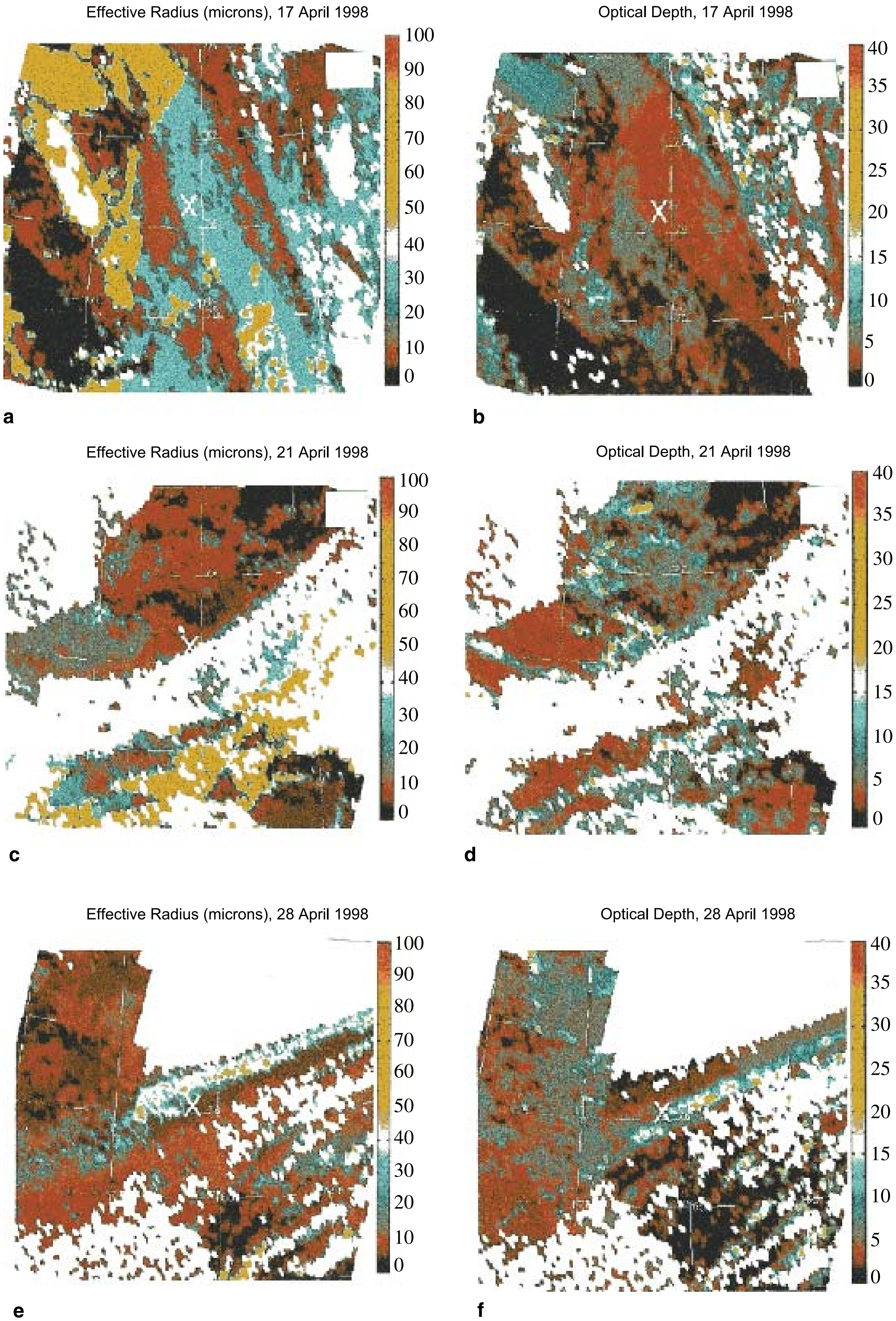

Fig. 9. Retrieved values of effective radius and optical thickness from NOAA AVHRR measurements for three cases. The cross shows the location of the ship. The area covered by the image is about $450 \times 480\,\mathrm{km}^2$

Table 4. Summary of AVHRR retrievals for three cases. r_{eff}, r_{effi}, τ, T_t, and h_t are effective size for droplets, effective size for ice crystals, optical thickness, and cloud top temperature and height, respectively. Subscript m, sd, min, max, and occ represent the mean, standard deviation, minimum, maximum, and occurrence, respectively

Cases	Parameter [x]	x_m	x_{sd}	x_{min}	x_{max}	N_p	f_{occ} for w/i < 50%	Mode of $\tau(f_{occ})$	h_t [km]
April 17	$R_{eff,w}$ [μm]	10.2	0.44	9.7	11.2	31	25%		
[76.12N	$R_{eff,i}$ [μm]	31.2	–	31.2	31.2	90	–	–	
165.46W]	τ	4.2	1.5	1.3	11.3	121	–	1.5 (80%)	0.5
	T_t [K]	261.6 (−11.5 °C)	0.4	260.2	262.3	121	–	–	
April 21	$R_{eff,w}$ [μm]	7.9	1.6	2.5	10.3	36	47%	–	
[76.08N	$R_{eff,i}$ [μm]	23.8	6.8	11.7	38.7	40	–	–	
165.51W]	τ	10.0	13.3	1.0	116.1	76	–	5 (70%)	3.1
	T_t [K]	253.9 (−19.3 °C)	1.2	251.8	255.8	76	–	–	
April 28	$R_{eff,w}$ [μm]	–	–	–	–	–	0%	–	
[75.99N	$R_{eff,i}$ [μm]	12.1	11.4	4.9	47.5	120	–	–	
166.18W]	τ	7.8	5.1	1.1	26.1	120	–	5 (42%)	3.5
	T_t [K]	248.4 (−24.8 °C)	2.7	243.3	253.3	120	–	–	

the large optical thickness. The d values around 0.5 show that most ice crystals were in irregular shapes. The values of d around 0.11–0.3 are for mostly single particles and $d < 0.11$ are for spherical particles (e.g., droplets; Sassen, 1991). Based on uncertainties in the optical properties of ice particles, these interpretations should be considered more qualitatively. For the 17 April case (Fig. 10c–d), a single persistent layer was observed for almost 4 hours. The B near ~75 indicates that this cloud was optically thick; therefore, high-clouds could not be detected. For the 21 April case (Fig. 10e–f), the d values were larger than 0.2, indicating that the cloud had a mixture of various ice crystal shapes. Large values of B above 2 km matched well with $d = 0.4$ values, indicating irregular ice crystals within the embedded convective cells. For the 28 April case, the cloud layer likely had many irregular particles and plates.

Ice crystal shape is an important parameter for remote sensing and cloud processes (Gultepe et al, 2000). For this reason, the depolarization ratio for the 28 April case (Fig. 10g) was determined for the entire cloud data. The results indicated that spherical particles and plates occur about 55% of the time, and single particles (e.g., columns plus aggregates/irregulars) occurred about 45% of the time.

5.5 MSC lidar depolarization and backscatter ratios

The MSC lidar collected data when the aircraft was above or below the cloud layer. The resolution of the MSC lidar was about 4 m in the vertical and ~100 m in the horizontal. Figure 11a–f shows the backscatter values (B) for the 16 April (a), 17 April (b), and 21 April (c) cases, for the indicated time periods, as well as two time periods for the 28 April (d and f). The depolarization ratio for 28 April is shown in Fig. 11e for the same time period as 28 April (d). These lidar runs were made nearby the SHEBA ship on the indicated days. There was a liquid layer observed at 2.5 km for the 16 April case. Cloud top was about 6 km. In this figure, the aircraft was above the cloud layer. The maximum B was 1000. Embedded structures (cells) with sizes of ~0.3–6 km are seen in the middle and high levels. For the 17 April case (b), a liquid layer was located below 0.5 km where the cloud base was at about 100 m. For the 21 April case (c), high values of B were seen close to the cloud base at about 1.3 km and the cloud top (B ~ 30) is about 3 km. At low levels, thin liquid clouds indicate that SHF and LHF from the refrozen leads likely played an important role for cloud formation. The cell sizes were about 0.1–3 km. For the 28 April case (d–f), the cloud vertical thickness was

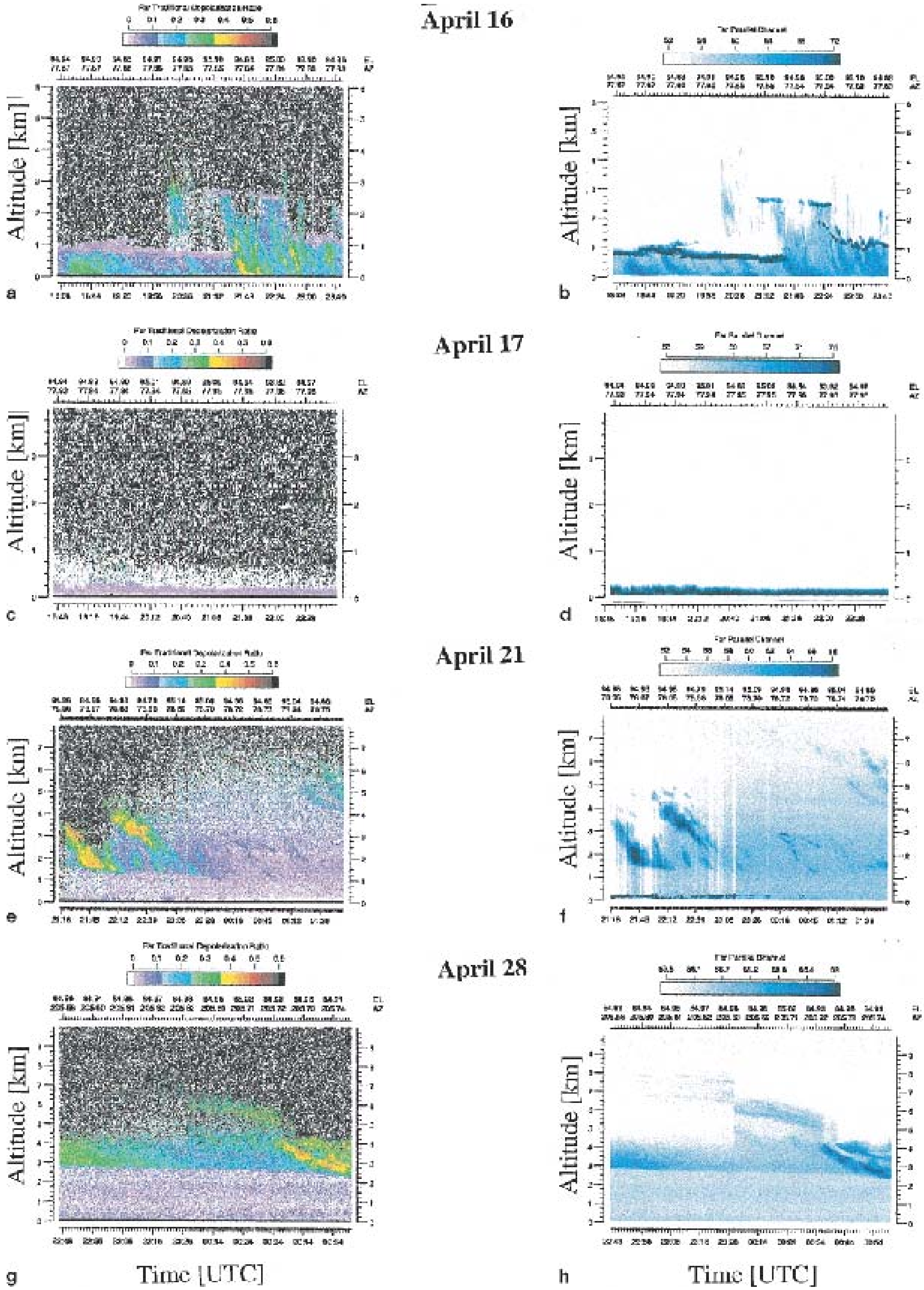

Fig. 10. Depolarization and backscatter ratio versus time obtained from NOAA DABUL for all cases

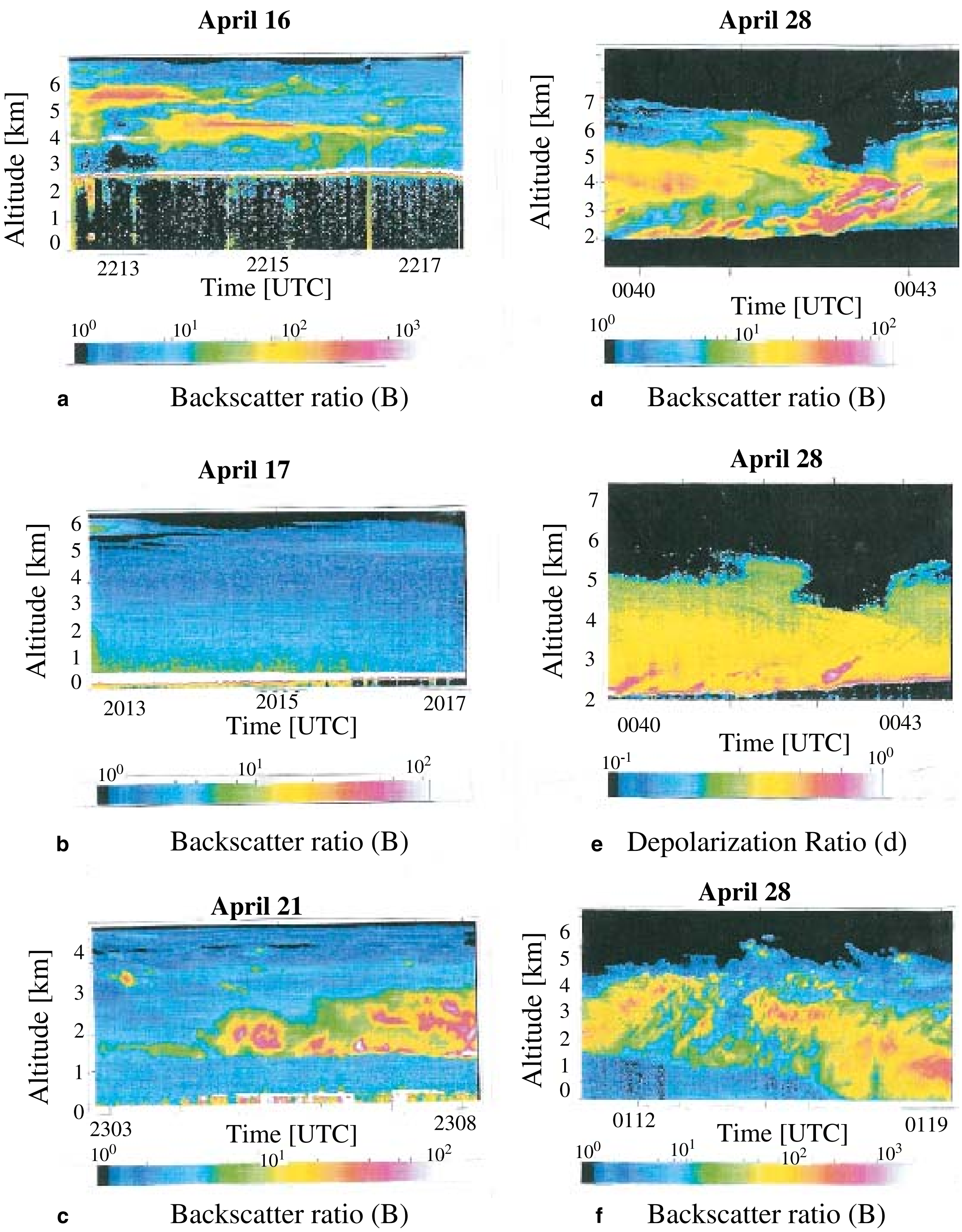

Fig. 11. Backscatter ratio from the MSC lidar for all cases are shown in boxes a, b, c, d, and e. The box f is for the depolarization ratio corresponding to backscatter ratio given in box e for only the 28 April case

larger compared to the other cases. Refrozen leads were observed at that time (Pinto et al, 2001). The B values greater than 100 represent the scales between 0.3 and 1.5 km (Fig. 11e). The depolarization ratio was greater than 0.2 (box e). Based on d values, ice crystals at the cloud top were likely plates, and they were mostly columns and irregulars in the other levels. The occurrence of irregular particle shape, in general, was well correlated with the region of embedded convective cells.

6. Discussions

In this section, comparisons between microphysical and dynamical parameters obtained from

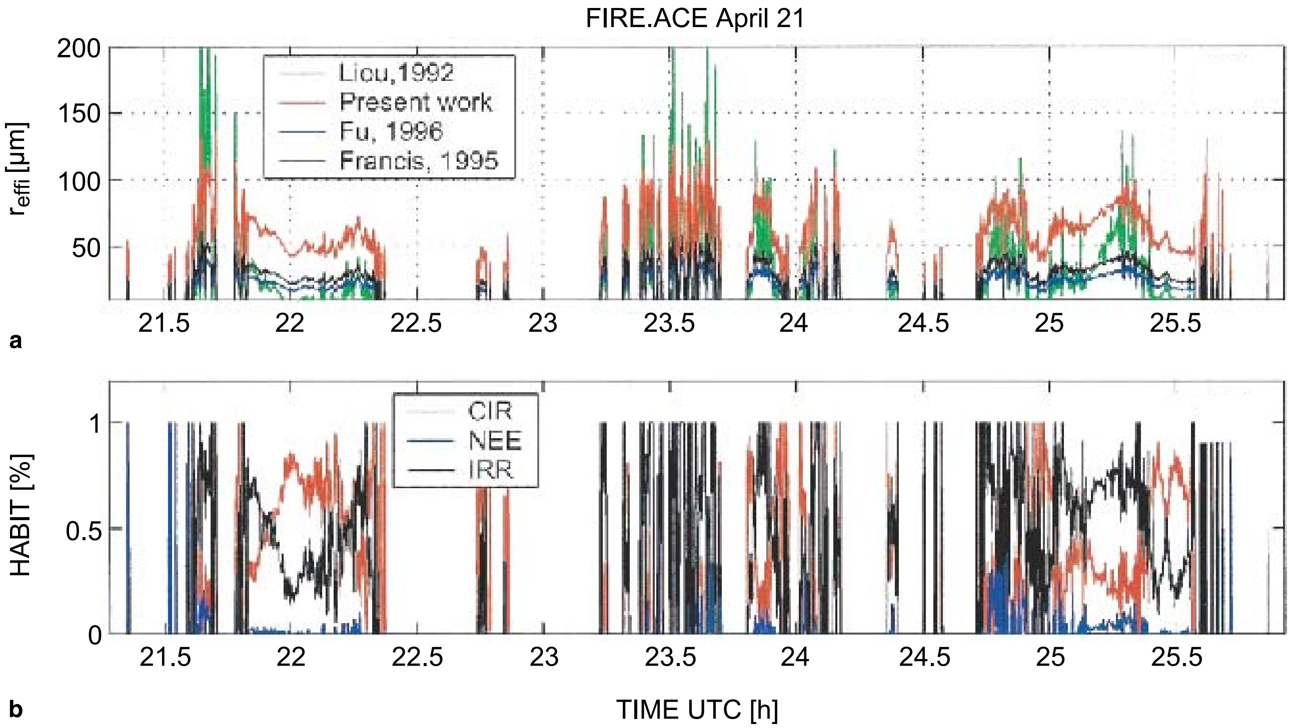

Fig. 12. Comparisons of $r_{effi2dc}$ obtained from in-situ data using various methods (**a**), and ice crystal shape occurrence (**b**) versus time for the 21 April case

various platforms are summarized. It should be noted that the sampling rate was different for each of the remote sensing platforms.

The effective size (r_{effi}) is derived from the aircraft 2D-C probe, using an equivalent volume assumption, a columnar particle shape (Liou, 1992), and an equivalent cross-section area (Francis, 1995; Fu, 1996). Comparisons of these results are shown in Fig. 12a. It shows that large differences occur between them. The r_{effi} obtained from the aircraft and AVHRR observations usually had a difference of less than 2 µm when Fu's method is used (not shown). The use of constant ice crystal density in Eq. (1) can be another source of uncertainty when *in-situ* measurements are compared with radar derived effective sizes. In general, ice crystal density is fixed in the satellite retrievals. These analyses indicate that, presently, without using aircraft data one cannot assess the accuracy of satellite observations. In fact, the columnar assumption in the retrieval of ice microphysical parameters cannot be accepted due to a large presence of irregular ice particles (Korolev et al, 1999). This can easily cause an uncertainty of 20–50% in the r_{eff} calculations (Francis, 1995; Gultepe et al, 2000). Irregular particles (based on in-situ measurements) occurred about 65–85% of the time (Fig. 12b), but this value is about 55% based on the NOAA lidar observations. Note that the ice particle shape frequency of occurrence cannot be obtained accurately when the shape of small ice particles is not precisely known (Lawson and Jensen, 1998). For the aircraft data, only particles with sizes considerably greater than 100 µm could be assigned a shape from the 2D-C probe measurements.

The difference in the phase ratio between the satellite and aircraft derived parameters can related to (1) the sampling areas/volumes were significantly different, and (2) the AVHRR is biased toward water clouds in the day time algorithm due to the dependence on the strong reflectance characteristics of water clouds at 3.7 µm. It is also possible that the aircraft-derived value is overestimated due to long flight segments made at low altitudes.

IWC is commonly used for climate studies and it can be obtained using the IWC-Z_e relationships (Sassen, 1987) or from a more detailed analysis (given in this work) of Doppler radar and microwave radiometers (Matrosov, 1997). Donovan et al (2001a; 2001b) combined lidar and radar observations to study cloud effective size and water content profiles and found that their retrieval results were comparable with in-situ, as well as infrared radiometer measurements. Unfortunately, use of such a retrieval method was not feasible during SHEBA because of the limited sensitivity of the remote sensing observations. The empirical relationships do not use ice crystal number concentration or size, rather, they depend on the reflectivity which is related to the 6th power of the particle size. If the ice crystal mass primarily exists within smaller sizes, that contribution to the IWC can be significant but the radar cannot detect these small particles, or biases its return to the few large particles. Similarly, the in-situ instruments (e.g., PMS 2D-C probe) cannot also accurately measure small particles with sizes less than 100 μm (Gultepe et al, 2001a). Therefore, a significant difference between aircraft and radar derived IWCs is found (Fig. 8). Note that the sampling volume of the aircraft instruments and the radar are quite different, which can also complicate the problem.

The NOAA lidar, similar to the MSC lidar, can detect cloud base or top heights, but when clouds become optically thick, they cannot be useful for collecting cloud data because the beam is strongly attenuated. On the other hand, the lidar can easily penetrate into clouds with smaller optical thickness. For many cases, Doppler radar could not see the cloud top height because reflectivity from the small particles was out of the radar detection range. A combination of both lidar and radar observations is the best way to detect cloud macro characteristics (Intrieri et al, 2000). Overall, monthly mean differences of the cloud top and base heights obtained from radar and lidar measurements can be about 3 km and 1 km, respectively (not shown), therefore, a combination of the radar-lidar method (Donovan et al, 2001) cannot not be used in the retrievals of microphysical parameters. Cloud top height and temperature differences from all platforms are summarized in Table 5. In this table, aircraft profiles represent a time period of about 20–25 minutes, not necessarily over the ship. The AVHRR derived cloud top characteristics represent an area of 50 km^2 and 45 minutes apart from radar and rawinsonde measurement times, therefore, cloud top heights (temperatures) should be used with care.

Table 5. Cloud top heights and temperatures from various platforms. Rawinsonde data are used to obtain temperatures for radar and heights for satellite

Days	Cloud top temperature [°C]				Cloud top height [km]			
	Rawinsonde 23:15 UTC	Radar/lidar 23:15 UTC (from Rawinsonde)	Aircraft (See Table 1 for time)	Satellite 24:00 UTC	Rawinsonde 23:15 UTC	Radar/lidar 23:15 UTC	Aircraft	Satellite 24:00 UTC (from Rawinsonde)
Apr. 16	−45	−43	−42	–	7.3	6.2	8.0	–
Apr. 17	−8	−7	−5	−11.5	0.6	0.4	0.5	0.5
Apr. 21	−33	−35	−23	−19.3	5.7	5.2	5.0	3.1
Apr. 28	−53	−47	−43	−24.8	10.5	8.5	7.1	3.5

Table 6. Sizes of the cells derived based on the measurements obtained from the various platforms

Case	Cell size [km]			
Platform	NOAA radar	MSC lidar	NOAA lidar	Aircraft
April 16	1–9	0.3–6	<2	0.003–2
April 17	0.1–3	–	–	0.003–2
April 21	0.5–1.5	0.1–3	<8	0.003–5
April 28	0.3–15	0.3–1.5	<1.5	0.003–10

The Doppler radar vertical velocities, due to alignment problems, may include a large uncertainty. The Doppler velocity (V_r) was always downward likely due to falling particles (Fig. 7). On the other hand, aircraft vertical air velocities for several segments reached more than $1\,m\,s^{-1}$ at scales of 3 m. In order to overcome such updrafts and to produce downward Doppler velocities, relatively large ice crystals must have been detected by the radar.

Cell sizes within the clouds were obtained using the mean plus sd values of related parameters (e.g., w, B, and d) for all cases (Table 6) for each platform. Then, any value in the time series greater than this critical value is assigned to cells. Note that here cells are defined as dynamically active regions. Because of the higher resolution, the aircraft measurements showed that cell sizes ranged from 3 m up to 10 km. The size of the cells determined from remote sensing platforms ranged from 0.3 km to 15 km. The Doppler radar was the most useful platform for detecting large cell sizes (~15 km). Differences between the observations obtained from various platforms were likely due to their sensitivity to particle size and concentration.

Pinto et al (1999), using the PAM (Portable Automated Mesonet) flux station measurements, studied a lead formed during the Convair-580 mission over the SHEBA ship. They calculated turbulent fluxes using a bulk aerodynamic formula. They found that SHF and LHF were less than $110\,W\,m^{-2}$ and $40\,W\,m^{-2}$, respectively. The values of SHF were 4 to 6 times greater than over the multiyear ice. Overall, these values were found comparable to those estimated from aircraft observations collected on 28 April (Fig. 3). Note that, although the comparisons made are acceptable, turbulent heat fluxes calculated from the in-situ data and bulk aerodynamic formula cannot be easily compared because of differences in the measurement levels and the variability in numerical "constants." The values of SHF smaller than $200\,W\,m^{-2}$ obtained from the ATI sonic anemometers and fast response temperature sensors (Pinto et al, 2001) were also found to be comparable to aircraft derived values (Fig. 3). Note that the averaging time for ATI measurements represents a 5-minute time period.

Aircraft observations indicate that the measurement uncertainties, assumptions made in the retrieval methods, as well as the variability in the measurements, and data collection time differences, can complicate comparisons between data from the aircraft and different remote sensing platforms.

7. Conclusions

The present study used observations obtained from multiple platforms, including aircraft, lidars, radar, and satellite. The uniqueness of the present data comes from the use of the limited observations collected over the SHEBA ship and integration of the observations obtained from multi-platforms over the various time and space scales. The integration of data sets from multiplatforms was the main aim of the SHEBA and FIRE.ACE field projects. The following conclusions were obtained from the present work.

(i) Dynamically active regions indicated that Arctic clouds can have embedded cells that can be a major source for significant turbulent heat fluxes (Pinto et al, 1995; Pinto, 1998). Calculated SHF and LHF show that Arctic clouds cannot always be stable, and inhomogeneity is significant when thermal and dynamical instabilities are present, especially where leads and polynyas are likely to be found (Andreas and Murfhy, 1986; Andreas et al, 1990).

(ii) The procedures described for AVHRR analysis are theoretically valid for homogeneous cloud systems with a single layer. Uncertainties in the retrieved parameters increase as clouds become less homogeneous. Results for multi-layer and multiphase clouds, and for single-layer clouds that are vertically and/or horizontally inhomogeneous, may be more representative of the upper portion of the cloud than the cloud layer as a whole.

(iii) The IWC calculation from IWC-Z_e and N_d from N_d–Z_e relationships can include a large uncertainty. This can be due to a large amount of undetected small ice crystals by the Doppler radar. In fact, IWC is related to the history of the vertical air velocity which currently cannot be accurately measured with the existing aircraft instrumentation (Gultepe and Starr, 1995; Gultepe et al, 1995).

(iv) The importance of vertical air velocity on N_i is discussed by Gultepe et al (2000). In the present study it is also shown that N_i becomes large when the absolute value of the vertical velocity becomes small. During a weak large scale lifting, small ice crystals form, then, they grow by diffusion. Particles fall out from the parcel while they reach a certain size. Weak large-scale lifting can easily be responsible for small IWC with large number concentrations and thus small particle sizes (Gultepe et al, 1995; Heymsfield, 1977). In this case, radar derived IWC values would be significantly underestimated.

(v) The depolarization values from the various platforms (e.g., lidars) suggest that its relationship to particle phase is still not well understood (Sassen, 1977; 1991; Intrieri et al, 2000). When circular ice particles are present, the depolarization ratio cannot be used for particle phase segregation.

Retrieval of particle size from satellite observations can be limited due to penetration of solar radiation in the optically thick clouds. This suggests that the upper part of the cloud layer is likely best represented in the satellite analysis.

(vi) Cloud top heights from all platforms showed a maximum difference up to 2 km, and rawinsonde cloud tops were usually greater than those of radar, satellite, and aircraft measurements. These differences are attributed to radar sensitivity, limitation of aircraft flight altitude, satellite retrieval method dependency on surface conditions, and time/space differences during the data collection times.

(vii) The r_{eff} for liquid clouds obtained from in-situ and satellite observations in the present study were comparable, indicating that the satellite's retrievals can be very useful for studying the distribution of r_{eff} over the Arctic region in large-scale models. In the mixed and only ice phase conditions, the retrieval method should be used with care because of unknown particle shape, size, concentration, and their optical characteristics (Gultepe et al, 2000; 2001b).

(viii) Differences between in-situ and radar derived effective sizes can be due to uncertainty in the small ice crystal number concentrations, fixed ice crystal density values, and inhomogeneity in the vertical air velocity field that is used in Doppler radar method.

(ix) In the 18 Canadian flights, including the SHEBA cases, mixed phase clouds can occur at about 30% of the time during April of 1998 (Gultepe et al, 2002). This is comparable to frequency of occurrence of liquid phase clouds in winter storms (Cober et al, 2001) that was likely due to unusually warm weather in Northern Canada in the spring of 1998.

(x) The phase change in the lower part of the clouds is generally related to a large heat transfer and relatively strong dynamic activity (e.g., w within the cloud). The cell sizes are estimated between 3–500 m and 15 km. In the corresponding scales, IWC values ranged from $0.1\,g\,m^{-3}$ to $0.001\,g\,m^{-3}$. This suggests that Arctic clouds have highly variable microphysical parameters that may significantly affect the energy budget of the Earth's atmosphere during the April transition times (Rotstayn, 1999a; 1999b).

The present study suggests that Arctic clouds should be studied using data obtained from various different platforms. Although it is not easy to process the various observations at the same time and space scales, the different measurement and integration techniques complement each other should be developed for better comparisons.

Acknowledgments

The Panel on Energy Research and Development provided financial support for Canadian participation within FIRE.ACE. Additional support was given from NASA for the collection of the FIRE.ACE data. The aircraft data were obtained using the National Research Council of Canada Convair-580 and the scientific and technical efforts of many NRC and MSC staff. The authors are also grateful to Dr. D. Wylie of University Wisconsin who provided weather forecasts during aircraft missions over the SHEBA ship. The 2D-C probe analysis was done using a software developed by S. Cober of AES. The authors wish to specifically thank Dave Marcotte of NRC for his leadership in preparing the Convair 580 for its field duties during FIRE.ACE.

References

Alvarez RJ, II, Eberhard WL, Intrieri JM, Sandberg SP, Koenig KW (1998) Cloud backscatter and phase measurements in the Arctic using ETL's DABUL lidar. Paper presented at the 4th Int. Symp. on Tropospheric Profiling, AMS, Snowmass, CO, September 20–25

Andreas EL, Murfhy B (1986) Bulk transfer coefficients for heat and momentum over leads and polynyas. J Phys Oceanogr 16: 1875–1883

Andreas EL, Miles MW, Barry RG, Schnell RC (1990) Lidar derived particle concentrations in plumes from Arctic leads. Ann Glaciol 24: 9–12

Baumgardner D, Cooper WA, Dye JE (1990) Optical and electronic limitations of the forward scattering spectrometer probe, liquid particle size measurements techniques, Vol. 2. ASTM STP 1083 (Dan Hirleman E, Bachalo WD, Felton PG, eds). American Society for Testing and Materials, Philadelphia, pp 115–127

Biter CJ, Dye JE, Huffman D, King WD (1987) The dropsize response of the CSIRO liquid water probe. J Atmos Ocean Tech 4: 359–367

Clarke JC, Mitrecu C, Cotton WR (1999) LES derived vertical air velocity spectra of fog and cirrus. 13th Symp. on Boundary Layers and Turbulence, Dallas, Texas, 10–15 January 1999, pp 208–211

Cober SG, Isaac GA, Korolev AV, Strapp JW (2000) Assessing the relative contributions of liquid and ice phases in winter clouds. Preprints, ISCCP Int. Cloud Physics Conf., Reno, Nevada, pp 689–692

Cober SG, Isaac GA, Korolev AV, Strapp JW (2001) Assessing cloud-phase conditions. J Appl Meteor 40: 1967–1983

Côté J, Gravel S, Methot A, Patoine A, Roch M, Staniforth A (1998) The operational CMC-MRB Global Environmental Multiscale (GEM) model, Part I: Design, considerations, and formulation. Mon Wea Rev 126: 1373–1395

Curry C (1983) On the formation of continental polar air. J Atmos Sci 40: 2278–2292

Curry JA, Rossow WB, Randall D, Schramm JL (1996) Overview of Arctic cloud and radiation characteristics. J Climate 9: 1731–1764

Curry JA, Hobbs PV, King MD, Randall DA, Minnis P, Isaac GA, Pinto JO, Uttal T, Bucholtz A, Cripe DG, Gerber H, Fairall CW, Garrett TJ, Hudson J, Intrieri JM, Jakob C, Jensen T, Lawson P, Marcotte D, Nguyen L, Pilewskie P, Rangno A, Rodgers D, Strawbridge KB, Valero FPJ, Williams AG, Wylie D (2000) FIRE Arctic clouds experiment. Bull Amer Meteor Soc 81: 5–29

Donovan DP, Van Lammeren ACAP, Hogan RJ, Russchenberg HWJ, Apituley A, Francis P, Testud J, Pelon J, Quante M, Goddard J (2001a) Cloud effective particle size and water content profile retrievals using combined lidar and radar observations 1. Theory and examples. J Geophy Res 106(D21): 27425–27448

Donovan DP, Van Lammeren ACAP, Hogan RJ, Russchenberg HWJ, Apituley A, Francis P, Testud J, Pelon J, Quante M, Goddard J (2001b) Cloud effective particle size and water content profile retrievals using combined lidar and radar observations 2. Comparison with IR radiometer and in-situ measurements of ice clouds. J Geophy Res 106(D21): 27449–27464

Francis P (1995) Some aircraft observations of the scattering properties of ice crystals. J Atmos Sci 8: 1142–1154

Frisch AS, Fairall CW, Snider JB (1995) Measurements of stratus cloud and drizzle parameters in ASTEX with a Ka-band Doppler radar and microwave radiometer. J Atmos Sci 52: 2788–2799

Fu Q (1996) The accurate parameterizations of the solar radiative properties of cirrus clouds for climate models. J Climate 9: 2058–2082

Fu Q, Liou KN (1993) Parameterization of the radiative properties of cirrus clouds. J Atmos Sci 50: 2008–2025

GEWEX News (1997) Satellite cloud data for regional studies 7(1)

Gultepe I, Isaac GA (2002) The effects of air-mass origin on Arctic cloud microphysical parameters during FIRE.ACE. J Geophy Res 107(C10): SHE 4.1–4.12

Gultepe I, Starr DO'C (1995) Dynamical structure and turbulence in cirrus clouds: Aircraft observations during FIRE. J Atmos Sci 52: 4060–4078

Gultepe I, Starr DO'C, Heymsfield AJ, Uttal T, Ackerman TP, Westphal DL (1995) Dynamical characteristics of cirrus clouds from aircraft and radar observations in micro and meso-gamma scales. J Atmos Sci 52: 4060–4078

Gultepe I, Isaac G, Hudak D, Nissen R, Strapp W (2000) Dynamical and microphysical characteristics of Arctic clouds during BASE. J Climate 13: 1225–1254

Gultepe I, Isaac GA, Cober SG (2001a) Ice crystal number concentration versus temperature for climate studies. Int J Climatol 21: 1281–1302

Gultepe I, Isaac GA, Strawbridge K (2001b) Variability of cloud microphysical and optical parameters obtained from aircraft and satellite remote sensing during RACE. Int J Climate 21(4): 507–525

Gultepe I, Isaac G, Williams A, Marcotte D, Strawbridge K (2003) Turbulent heat fluxes over leads and polynyas and their effect on Arctic clouds during FIRE-ACE: Aircraft observations for April 1998. Atmos Ocean 41(1): 15–34

Heymsfield AJ (1977) Precipitation development in stratiform ice clouds: A microphysical and dynamical study. J Atmos Sci 34: 367–381

Heymsfield AJ, Parrish JL (1978) A computational technique for increasing the effective sampling volume of the PMS two-dimensional particle size spectrometer. J Appl Meteor 17: 1566–1572

Intrieri JM, McCarty BJ, Eberhard WL, Alvarez RJ (2000) Liquid water phase in the Arctic atmosphere. Symp. on Lidar Atmospheric Monitoring, January 9–14, 2000, Long Beach, CA, Amer Meteor Soc, Boston, Mass, pp 40–43

Intrieri JM, Shupe MD, Uttal T, McCarty BJ (2002) An annual cycle of Arctic cloud characteristics observed by radar and lidar at SHEBA. J Geophys Res 107(C10): 8030, DOI 10.1029/2000JC000423

Jensen EJ, Toon OB, Westphal DL, Kinne S, Heymsfield AJ (1994) Microphysical modeling of cirrus 2. Sensitivity studies. J Geophy Res 99: 10443–10454

Kantha LH (1995) A numerical model of Arctic leads. J Geophy Res 100: 4653–4672

Key J (1995) Retrieval of cloud optical depth and particle effective radius at high latitudes using visible and thermal satellite data. Proc. Europ. Symp. on Satellite Remote Sensing II, Paris, September, SPIE Vol. 2578, pp 318–325

Key J (2000) The cloud and surface parameter retrieval (CASPR) system for polar AVHRR. Cooperative Institute for Meteorological Satellite Studies, University of Wisconsin, Madison, 59 pp

Key J, Intrieri J (2000) Cloud particle phase determination with the AVHRR. J Appl Meteor 1797–1804

Key J, Schweiger AJ (1998) Tools for atmospheric radiative transfer: Streamer and FluxNet. Comp Geosci 24(5): 443–451

Key J, Yang P, Baum BA, Nasiri SL (2002) Parameterization of shortwave ice cloud optical properties for various particle habits. J Geophy Res (forthcoming)

Korolev AV, Isaac GA, Hallett J (1999) Ice particle habits in Arctic clouds. Geophy Res Lett 26: 1299–1302

Lawson RP, Jensen TL (1998) Improved microphysical observations in mixed phase clouds. Preprints Conf. on Cloud Physics, 17–21 August, Everett, Washington, pp 451–454

Liou KN (1992) Radiation and cloud processes in the atmosphere: Theory, observation, and modeling. New York: Oxford University Press, 487 pp

Liu PSK, Leaitch WR, Banic CM, Li S-M (1996) Aerosol observations at Chebogue Point during the 1993 North Atlantic Regional Experiment: Relationships among cloud condensation nuclei, size distribution, and chemistry. J Geophy Res 101: 28971–28990

Matrosov SY (1997) Variability of microphysical parameters in high-altitude ice clouds: Results of the remote sensing method. J Appl Meteor 36: 633–648

Matrosov SY (1999) Retrievals of vertical profiles of ice cloud microphysics from radar and IR measurements using tuned regressions between reflectivity and cloud parameters. J Geophy Res 104: 16741–16753

Matrosov SY, Heymsfield AJ (2000) Use of Doppler radar to assess ice cloud particle fall velocity-size relations for remote sensing and climate studies. J Geophy Res 105: 22427–22436

Matrosov SY, Heymsfield AJ, Kropfli RA, Martner BE, Reinking RF, Snider JB, Piironen P, Eloranta EW (1998) Comparisons of ice cloud parameters obtained by combined remote sensor retrievals and direct methods. J Atmos Ocean Tech 184–196

Matrosov SY, Korolev AV, Heymsfield AJ (2002) Profiling cloud ice mass and particle size from Doppler radar measurements. J Atmos Ocean Tech 19: 1003–1018

McInnes KL, Curry JA (1995) Modeling the mean and turbulent structure of the summertime Arctic cloudy boundary layer. Bound Layer Meteorol 73: 125–143

Moran KP, Martner BE, Post MJ, Kropfli RA, Welsh DC, Widener KB (1998) An unattended cloud-profiling radar for use in climate research. Bull Amer Meteor Soc 79: 443–455

Murad PD, Walter BA (1996) Analysis of meso-scale linear features observed in the Arctic atmospheric boundary layer. Mon Wea Rev 124: 1924–1940

Nakajima T, King MS (1990) Determination of the optical thickness and effective particle radius of clouds from reflected solar radiation measurements. Part I: Theory. J Atmos Sci 47: 1878–1893

NOAA, 1991, NOAA Polar Orbiter Data User's Guide. U.S. Dept. of Commerce, National. Ocean. and Atmos. Admin., NESDIS, February, 289 pp

Pinto JO (1998) Autumnal mixed-phase cloudy boundary layers in the Arctic. J Atmos Sci 55: 2016–2038

Pinto JO, Curry JA (1995) Atmospheric convective plumes emanating from leads: II. Microphysical and radiative processes. J Geophy Res 100(C3): 4633–4642

Pinto JO, Curry JA, McInnes KL (1995) Atmospheric convective plumes emanating from leads 1. Thermodynamic structure. J Geophy Res 100: 4621–4631

Pinto JO, Maslanik JA, Guest PS, Stone RS, Andreas EL, Fairall CW, Persson POG (1999) Surface energy budget and atmospheric effects of a freezing lead at SHEBA. 13th Symp. on Boundary Layers and Turbulence, Dallas, Texas, pp 519–522

Pinto JO, Alam A, Maslanik JA, Tschudi MA, Curry JA (2001) Surface characteristics and atmospheric footprint of springtime Arctic leads at SHEBA. J Geoph Res (forthcoming)

Randall D, Curry J, Battisti D, Flato G, Grumbine R, Hakkinen S, Martinson D, Preller R, Walsh J, Weatherly J (1998) Status of and outlook for large-scale modelling of atmosphere-ice-ocean interactions in the Arctic. Bull Amer Meteor Soc 79: 197–209

Rao CRN, Degradation of the visible and near-infrared channels of the advanced very high-resolution radiometer on the NOAA-9 spacecraft: Assessment and recommendations for corrections. NOAA Technical Report NESDIS 70, U.S. Department of Commerce, 25 pp

Roger JC, Vermote EF (1998) A method to retrieve the reflectivity signature at 3.75 μm from AVHRR. Rem Sens Environ 64: 103–114

Rotstayn LD (1999a) Climate sensitivity of the CSIRO GCM: Effect of cloud modelling assumptions. J Climate 12: 334–356

Rotstayn LD (1999b) Indirect forcing by anthropogenic aerosols: A global climate model calculation of the effective-radius and cloud-lifetime effects. J Geophys Res 104: 9369–9380

Sassen K (1977) Ice crystal habit discrimination with the optical backscatter depolarization ratio. J Appl Meteor 16: 425–431

Sassen K (1987) Ice cloud content from radar reflectivity. J Clim App Met 26: 1050–1053

Sassen K (1991) The polarization lidar technique for cloud research: A review and current assessment. Bull Amer Meteor Soc 72: 1848–1866

Schnell RC, Barry RG, Miles MW, Andreas EL, Radke LF, Brock CA, McCormick MP, Moore JL (1989) Lidar detection of leads in Arctic sea ice. Letters to Nature 339: 530–532

Serreze MC, Maslanik JA, Rehder MC, Schnell RC (1992) Theoretical heights of buoyant convection above open leads in the winter pack ice cover. J Geophys Res 97: 9411–9422

Shupe MD, Uttal T, Matrosov SY, Frisch AS (2002) Cloud water contents and hydrometeor sizes during the FIRE-Arctic clouds experiment. J Geophys Res (forthcoming)

Smith PC, MacPherson JI (1996) Airborne surveys of the atmospheric boundary layer above the marginal ice zone on the Newfoundland shelf. Atmos Ocean 34: 161–184

Spinhirne JD, Hart WD (1990) Cirrus structure and radiative parameters from airborne lidar and spectral radiometer observations: 28 October 1986 FIRE-case study. Mon Wea Rev 118: 2329–2343

Strapp JW, Chow P, Maltby M, Bezer AD, Korolev A, Stromberg I, Hallett J (1999) Cloud microphysical measurements in thunderstorm outflow regions during Allied/BAE 1997 flight trials. Preprints, 37th AIAA Aerospace Sciences Meeting and Exhibit, January 11–14, 1999, Reno, NV

Strawbridge KB, Harwood MG (1998) Preliminary airborne lidar results in the Canadian Arctic during FIRE III. Proc. SPIE Optical Remote Sensing of Atmosphere and Clouds, V. 3501, Beijing, China, pp 134–141

Williams A, Marcotte D (1999) Wind measurements on a maneuvering twin-engine turboprop aircraft accounting for flow distortion. J Atmos Ocean Tech 17: 795–810

Xiong WX, Li, Lubin D, Stamnes K (2002) Evaluating the principles of cloud remote sensing with AVHRR and MAS imagery over SHEBA. J Geophys Res (forthcoming)

Authors' addresses: I. Gultepe (E-mail: ismail.gultepe@ec.gc.ca) and G. A. Isaac, Meteorological Service of Canada, Cloud Physics Research Division, 4905 Dufferin St., Toronto, Ontario, M3H-5T4, Canada; J. Key, National Environmental Satellite, Data, and Information Service, National Oceanic and Atmospheric Administration, 1225 West Dayton St., Madison, WI 53706, USA; J. Intrieri, NOAA/Environmental Technology Laboratory, 325 Broadway, Boulder, CO 80303, USA; D. O'C. Starr, NASA Goddard Space Flight Center, Code 913, Greenbelt, MD 20771, USA; K. B. Strawbridge, Air Quality Processes Research Division, Meteorological Service of Canada, R-R#1, Egbert, Ontario, L0L IN0, Canada